Time-lapse monitoring of seismic velocity associated with 2011 Shinmoe-dake eruption using seismic interferometry: an extended Kalman filter approach

Kiwamu Nishida[1], Yuta Mizutani[1,2], Mie Ichihara[1], Yosuke Aoki[1]

[1]Earthquake Research Institute, University of Tokyo, 1-1-1 Yayoi 1, Bunkyo-ku, Tokyo 113-0032, Japan
[2]JX Nippon Oil & Gas Exploration Corp.

Key Points:

- A new technique of an extended Kalman filterz for estimating the temporal change of seismic velocity is developed.
- Mass variations in the subsurface due to precipitation can explain observed seasonal variations in seismic velocity.
- Spatial and temporal variations in seismic velocity suggest that damage due to magma migration could be the origin.

Corresponding author: Kiwamu Nishida, knishida@eri.u-tokyo.ac.jp

Abstract

Seismic interferometry is a powerful tool to monitor the seismic velocity change associated with volcanic eruptions. For the monitoring, changes in seismic velocity with environmental origins (such as precipitation) are problematic. In order to model the environmental effects, we propose a new technique based on a state-space model. An extended Kalman filter estimates seismic velocity changes as state variables, with a first-order approximation of the stretching method. We apply this technique to three-component seismic records in order to detect the seismic velocity change associated with the Shinmoe-dake eruptions in 2011 and 2018. First, ambient noise cross-correlations were calculated from May 2010 to April 2018. We also modeled seismic velocity changes resulting from precipitation and the 2016 Kumamoto earthquake, with exponential type responses. Most of the results show no significant changes associated with the eruptions, although gradual inflation of the magma reservoir preceded the 2011 eruption by one year. The observed low sensitivity to static stress changes suggests that the fraction of geofluid and crack density at about 1 km depth is small, and the crack shapes could be circular. Only one station pair west of the crater shows the significant drop associated with the eruption in 2011. The gradual drop of seismic velocity up to 0.05% preceded the eruption by one month. When the gradual drop began, volcanic tremors were activated at about 2 km depth. These observations suggest that the drop could be caused by damage accumulation due to vertical magma migration beneath the summit.

1 Introduction

Shinmoe-dake forms part of a group of Kirishima volcanoes, located in Kyusyu Japan, and is an active volcano. Over a period of ten years, it experienced a major eruption in 2011, and a effusive eruption in 2018. In 2011, the eruptive sequence started with sub-Plinian eruptions (January 26-27th), followed by a lava effusion (January 28-31st), and culminating in Vulcanian eruptions (1-10 Feb.) (Nakada et al., 2013). Observations from Global Navigation Satellite Systems (GNSS) show that the gradual inflation of the magma reservoir preceded the 2011 eruption by one year. The magma reservoir is located approximately 7 km northwest of Shinmoe-dake at a depth of approximately 8 km below sea level (BSL) (Nakao et al., 2013; Kozono et al., 2013). When the inflation started, low-frequency earthquakes (LFE) at a depth of 20-27 km was activated, suggesting the migration of magma from a deeper region (Kurihara et al., 2019). During the 2011 eruptions, the GNSS data indicate the co-eruption deflation of the magma reservoir. Tilt observation showed an-hour-long inflation and rapid deflation at a shallow depth (around 500 m) near the summit right before the first sub-Plinian event (Takeo et al., 2013). Also stepwise local tilt inflations were reported twice in about a week before the sub-Plinian event (Ichihara & Matsumoto, 2017). During the eruption, explosion earthquakes were observed (Nakamichi et al., 2013). The activities suggest that the magma touched an aquifer at shallow depths of about -1.0 km BSL (e.g., Kagiyama et al., 1996). Before and during the sub-Plinian eruptions, migration of gas (probably with magma) also activated continuous volcanic tremors (Ichihara & Matsumoto, 2017). These were located beneath the crater for one week before the major eruption, and they rose from a depth of a few kilometers to the near-surface aquifer three times. The heat transported to the water layer could have triggered the sub-Plinian eruptions (Ichihara & Matsumoto, 2017). In order to understand the magma plumping system, pertinent information from depths of 1 to 10 km is crucial. However, we could not detect earthquake activity at these depths before the major eruptions associated with the magma migration (Ueda et al., 2013) and other geophysical phenomena.

Seismic interferometry is a powerful technique for monitoring seismic velocity in the depth range of interest. In recent years, the number of applications of seismic interferometry has increased. In the analysis, the cross-correlation function between ambient noise records of a pair of stations can be regarded as a virtual seismic waveform, recorded

at one station when the source is placed at the other station. In any time period, the seismic velocity around the station pair can be estimated from the cross-correlation function calculated without an earthquake; thus, seismic interferometry has been applied in many studies to monitor temporal changes in seismic velocity (e.g., Obermann & Hillers, 2019). This technique has been applied for detecting seismic wave velocity changes after large earthquakes (e.g., Wegler & Sens-Schönfelder, 2007; Wegler et al., 2009; Brenguier, Campillo, et al., 2008; Brenguier et al., 2014), those of a slow slip event (Rivet et al., 2011), and those associated with volcanic eruptions: e.g., the Piton de La Fournaise volcano, La Réunion, France (Brenguier, Shapiro, et al., 2008), Mt. Asama, Japan (Nagaoka et al., 2010), Merapi volcano, Indonesia (Budi-Santoso & Lesage, 2016), Ubinas volcano, Peru (Machacca et al., 2019), and Kilauea volcano, USA (Donaldson et al., 2017). For example, Brenguier, Shapiro, et al. (2008) detected a drop in seismic velocity of the order of 0.1% for a number of days preceding the eruption of the Piton de La Fournaise volcano, and the velocity recovered at a time scale of about 10-20 days. There are two potential mechanisms for the temporal changes (Olivier et al., 2019). The first is pressurization due to the magma migration in a linear elastic regime. In this regime, stress sensitivity of seismic velocity change is a proxy for inferring the state of the material: in particular the existence of geofluid (Brenguier et al., 2014). The second is damage accumulation beyond the linear elastic regime.

The biggest technical difficulty in monitoring is the separation of temporal variations of volcanic origin from environmental variations. Many researchers reported seasonal variations associated with environmental phenomena: rainfall (e.g., Rivet et al., 2015), air pressure (e.g., Niu et al., 2008), and thermo-elasticity (e.g., Hillers, Ben-Zion, et al., 2015). In the region of Mt. Shimoe-dake, daily precipitation exceeds 100 mm for several days in a year, while the annual precipitation is more than 4000 mm. Wang et al. (2017) reported that rainfall is the major source of the observed temporal changes in this area (Kyusyu). The Merapi Volcano, Indonesia, Sens-Schönfelder and Wegler (2006) also experienced the observed dominance of seasonal variations. Temporal changes in groundwater levels based on precipitation data can explain the observed strong seasonal variations in both cases. Such strong seasonal variations have the potential to mask a temporal change associated with volcanic activities; thus, correction for rainfall is crucial for inferring the temporal changes associated with volcanic activity (Rivet et al., 2015; Wang et al., 2017).

Earthquakes also contaminate temporal changes in seismic velocities associated with volcanic activities. In particular, this region experienced the 2016 Kumamoto earthquake of Mw 7.3 (e.g., Kato et al., 2016). The seismic-velocity dropped during the earthquake, and recovered over a time scale of several months (Nimiya et al., 2017). Since the seismic-velocity reduction on the order of 0.1% could be comparable to typical temporal variations associated with volcanic activities, it should be subtracted. Moreover, the susceptibility, which is defined by the ratio between observed reductions in seismic velocity and the estimated dynamic stress (Brenguier et al., 2014), is a good proxy for discussing the state of geofluid in the upper crust associated with a volcanic process.

In this study, we introduce an empirical Bayes approach to separate the effects of precipitation and the earthquake from the observed seismic velocity changes to extract those of volcanic origins (Malinverno & Briggs, 2004). It has two levels of inference. At the lower level, the seismic velocity changes were modeled in a state-space form. An extended Kalman filter/smoother (section 4) estimates seismic velocity changes as state variables. Precipitation and earthquake effects are modeled as explanatory variables, which are deterministic at this level. At the higher level, hyper-parameters (model covariance, data covariance, and explanatory variables) are estimated by the Maximum Likelihood Method (section 5). This two-level approach has the following features: (1) we can constrain the hyper-parameters from data directly. (2) we can evaluate the separation of the origins in a statistical manner, (3) the approach gives us a criterion of the model selec-

tion (see section 5.3 for details) and (4) the extended Kalman filter/smoother is numerically efficient. Notation section at the end of this paper provides a list of definitions of the variables used in this paper.

We combine the extracted temporal velocity changes of volcanic origins with the geodetic observation and volcanic tremor activity to discuss the magma migration in section 6.

2 Cross-correlation analysis

We used three component seismograms recorded at eight stations (six broadband sensors and two short-period sensors with a natural frequency of 1 Hz) from May 1st, 2010 to April 30th, 2018, shown in Figure 1. Five stations were deployed by the Earthquake Research Institute, the University of Tokyo, and the other three were deployed by the National Research Institute for Earth Science and Disaster Prevention (NIED). The details of the sensors are shown in Table 1. We used daily precipitation data recorded by a station (Ebino shown by the white circle in Figure 1) of the Japan Meteorological Agency (JMA) for correcting the precipitation effects as described in section 5.1.

First, the data were down-sampled from 100 Hz to 2.5 Hz. The instrumental responses were corrected in time domain (Maeda et al., 2011) according to the sensor type, and all records were bandpass-filtered from 0.15 to 0.90 Hz. For each station pair, the two horizontal components were rotated into radial and transverse coordinates according to the geometry of the station pair: the radial direction is parallel to the great circle path between the station pair, and the transverse direction is perpendicular to the great circle path (Nishida et al., 2008). The daily records were divided into segments of 409.6 s, with an overlap of 204.8 s.

To reject noisy data, which include transient phenomena such as high instrumental noise or earthquakes, we discarded the noisy segments as follows. For one-day data of each component at a station, we estimated the root mean squared amplitudes (RMSs) of all the segments. For each component of one-day data, we defined the threshold to be twice the median value of RMSs for all the segments in one day. If the RMS of a segment was larger than the threshold, the segment was discarded.

Network	Station name	Sensor type
ERI	KVO	L4-C (1 s, -2/2/2011), Trillium-120 (120 s, 2/3/2011-)
ERI	SMN	Trillium-40 (40 s, -7/22/2010) Trillium-120 (120 s, 7/23/2010-)
ERI	SMW	L4-C (1 s)
ERI	TKW	CMG3T (100 s)
ERI	TKS	Trillium-40 (40 s, -2/4/2011) Trillium-120 (120 s, 2/5/2011-)
NIED (V-net)	KRHV	Trillium-240 (240 s)
NIED (V-net)	KRMV	Trillium-240 (240 s)
NIED (Hi-net)	MJNH	Hi-net 1 Hz velocity meter (1 s)

Table 1. Sensor type for each station. ERI represents a station deployed by the Volcano Research Center, Earthquake Research Institute, the University of Tokyo. NIED (V-net) means a station of the Volcano Observation network deployed by the National Research Institute for Earth Science and Disaster Prevention, and NIED (Hi-net) means a station of High-Sensitivity Seismograph Network deployed by NIED.

We then took cross-correlation functions (CCFs) of all possible pairs of stations, and all possible component combinations for each station pair with the spectral whiten-

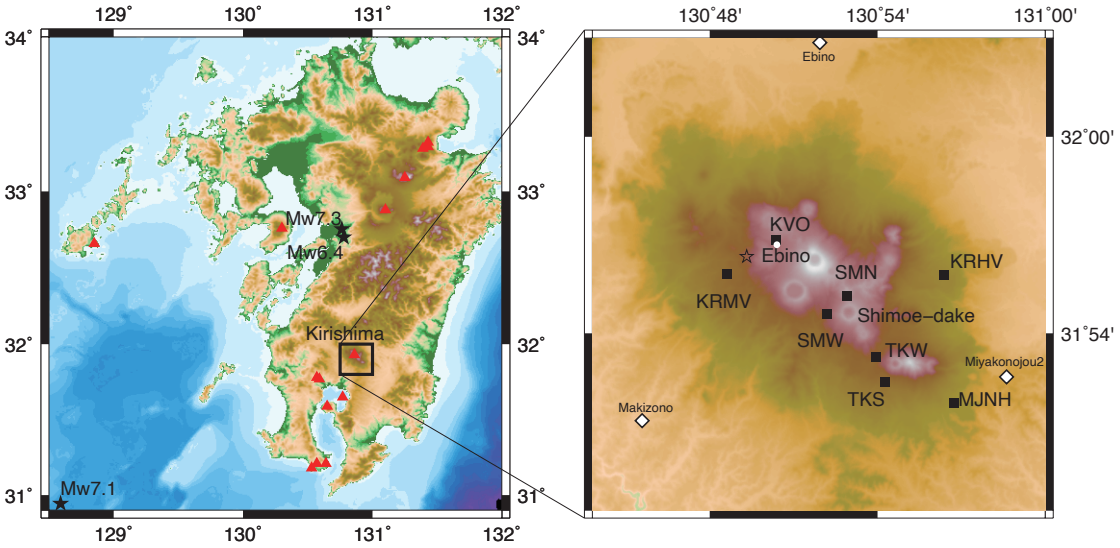

Figure 1. Left: Red triangles show active volcanoes. Black stars represent the hypocenters of earthquakes: (i) Mw 6.4, April 14th (UTC), 2016, the foreshock of the Kumamoto earthquake, (ii) Mw 7.3, April 15th (UTC), 2016, the mainshock of the Kumamoto earthquake and (ii) Mw 7.1, November 13th (UTC), 2015, the Satsuma earthquake. Right: Station distribution. Black squares show station locations, and the white circle shows the JMA weather station. Three white diamond symbols show the locations of GEONET stations operated by the Geospatial Information Authority of Japan. The star symbol shows the location of a volumetric source at a depth of 8.35 km (Nakao et al., 2013). The topography in the right panel is given by the corresponding Shuttle Radar Topography Mission (Farr et al., 2007).

ing, as done in previous studies (Bensen et al., 2007). We stacked the CCFs of the selected segments over one day. The daily CCFs of the individual pairs of stations were represented by $\phi_t^p(\tau)$, where τ shows lag time, and the subscript t is an integer, which represents days from 1 May 2010 (JST), and the superscript p shows the pair of components (9 components: $R-R$, $R-T$, ..., $Z-Z$, where R is the radial component, and T is transverse component, and Z is vertical component). Figure 2 shows a typical example of daily CCFs, which are stable even in their coda parts for eight years. Figure 3 shows a typical example of the mean power spectrum of the mean CCF between a pair of broadband stations, which shows dominance in lower frequencies from 0.25-0.5 Hz, even after the spectral whitening.

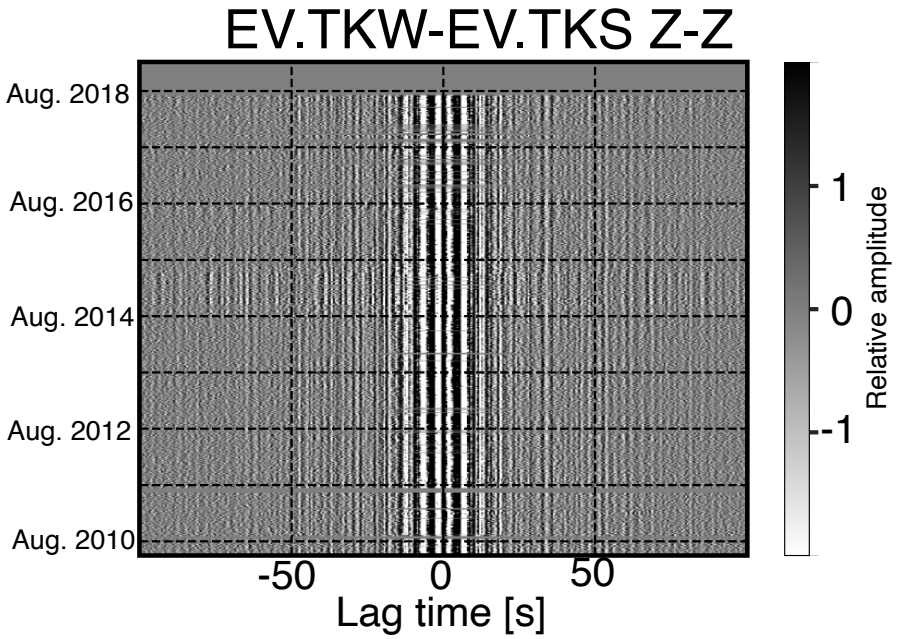

Figure 2. Daily CCFs of Z-Z component (0.2-0.4 Hz) between TKS and TKW. The vertical axis shows date, the horizontal axis shows lag time.

3 Measurements of seismic velocity change

Seismic interferometry is feasible for monitoring seismic wave velocity between pairs of stations. The principle of seismic interferometry is that the CCF between a station pair represents the seismic wavefield as though a source lies at one station and a receiver lies at the other. However, the disadvantage of this technique is that the measurements are overly sensitive to source heterogeneity (e.g., Weaver et al., 2009). This causes a trade-off between a temporal change of seismic velocity and that of source heterogeneity. Although the direct waves are sensitive to the source heterogeneity, the coda part becomes insensitive with increasing lapse time. This is because the seismic wavefield loses the source information over multiple scatterings (Colombi et al., 2014). If the seismic velocity changes uniformly in space, the arrival time delays with lapse time. This approach is known as the doublet method in frequency domain, first applied to earthquake coda (Poupinet et al., 1984). This method is also feasible for monitoring of seismic velocity with seismic interferometry (e.g., Brenguier et al., 2014; Hillers, Husen, et al., 2015). We used the method in the time domain, known as the stretching method (Weaver & Lobkis, 2000), because

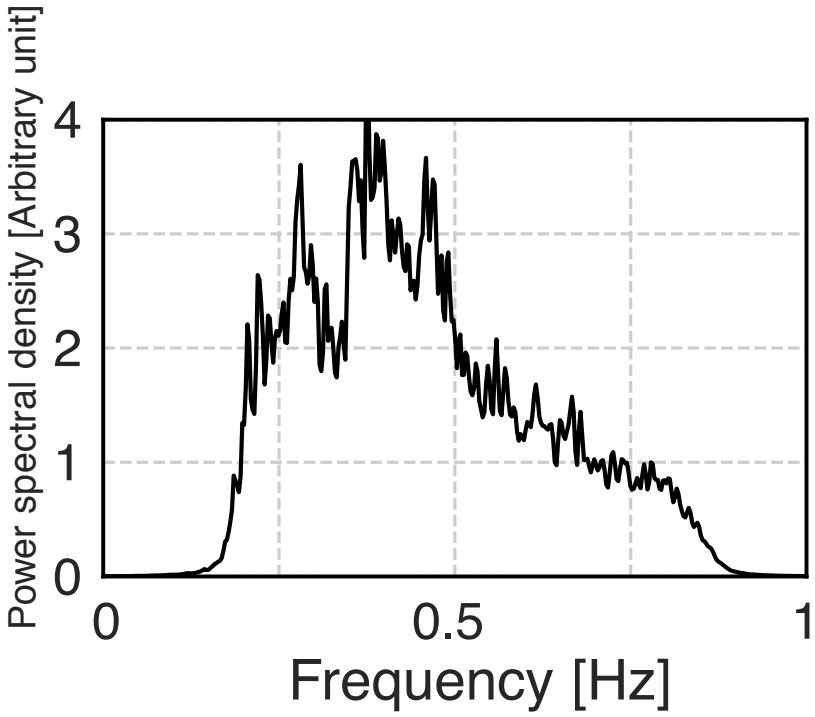

Figure 3. Power spectrum averaged over all CCFs between TKS and TKW with the time window from -99.6 to -20 s and from 20 to 99.6 s.

the linearization is easier for an application of an extended Kalman filter as described in the next section.

We constructed a model function, $m^p(A_t, \gamma_t; \tau)$, for the observed CCF $\phi_t^p(\tau)$ by stretching the reference CCF $\varphi_{ref}^p(\tau)$ as,

$$m^p(A_t, \gamma_t; \tau) = A_t \varphi_{ref}^p(\tau(1 + \gamma_t)), \tag{1}$$

where γ_t is the stretching factor, A_t is amplitude and the subscript t represents day. The preliminary reference CCF $\varphi_{ref}^p(\tau)$ was estimated by averaging all the observed CCFs $\phi_t^p(\tau)$ over days t (see section 4.1).

To estimate the temporal evolution of γ_t, Weaver and Lobkis (2000) constructed a dilation correlation coefficient between waveforms X^p as,

$$X^p(\gamma_t) = \frac{\int \phi_t^p(\tau) m^p(A_t, \gamma_t; \tau) d\tau}{\sqrt{\int \phi_t^p(\tau)^2 d\tau} \sqrt{\int (m^p(A_t, \gamma_t; \tau))^2 d\tau}}. \tag{2}$$

By maximizing the correlation, the temporal variation γ_t can be estimated. Several researchers have used this method to measure the temporal changes in seismic velocity. To enhance the signal to noise ratio, measurements over many station pairs and components were averaged. Bayesian approaches (Tarantola & Valette, 1982) for these measurements are feasible for more reliable estimations (Brenguier et al., 2016).

To enhance the flexibility of the Bayesian approach, we developed a new method of an extended Kalman filter based on the state-space model (e.g., Segall & Matthews, 1997; Durbin & Koopman, 2012). This method, successively, minimizes the squared difference given by

$$S(A_t, \gamma_t) \equiv \int \left(\phi_t^p(\tau) - m^p(A_t, \gamma_t; \tau)\right)^2 d\tau. \tag{3}$$

A_t and γ_t are recognized as state variables for the state modeling as shown in the next section.

In sections 4 and 5, we introduce an empirical Bayes approach to minimize the squared difference. It has two levels of inference. At the lower level, the seismic velocity changes were modeled in a state-space form. An extended Kalman filter/smoother (section 4) estimates seismic velocity changes as state variables. At the higher level, hyper-parameters (model covariance, data covariance, and explanatory variables for precipitation and earthquake effects) are estimated by the Maximum Likelihood Method (section 5).

4 State Space modeling using an extended Kalman filter approach

Here we considered state variables $\boldsymbol{\alpha}_t$, which describe the amplitude A_t and the stretching factor γ_t at $t = 1, \ldots, n$ assuming that the state variables are common to all the 9 components for each station pair. The state variables and the data vector of observed CCF $\boldsymbol{y}_t^p$ for a pth component are defined by

$$\boldsymbol{\alpha}_t \equiv \begin{pmatrix} A_t \\ \gamma_t \end{pmatrix}, \boldsymbol{y}_t^p \equiv \begin{pmatrix} \phi_t^p(-\tau_e) \\ \vdots \\ \phi_t^p(-\tau_s) \\ \phi_t^p(\tau_s) \\ \vdots \\ \phi_t^p(\tau_e) \end{pmatrix}, \tag{4}$$

where τ_s is the start of lag time (20 s) and τ_e is the end of lag time (99.6 s). They obey the following relations:

$$\boldsymbol{y}_t^p = \boldsymbol{m}^p(\boldsymbol{\alpha}_t + \boldsymbol{R}_t + \boldsymbol{E}_t) + \boldsymbol{\epsilon}_t, \qquad \boldsymbol{\epsilon}_t \sim \mathcal{N}(0, \boldsymbol{H}_t) \tag{5}$$

$$\boldsymbol{\alpha}_{t+1} = \boldsymbol{\alpha}_t + \boldsymbol{\eta}_t, \qquad \boldsymbol{\eta}_t \sim \mathcal{N}(0, \boldsymbol{Q}_t). \tag{6}$$

Here we introduce explanatory variables $\boldsymbol{R}_t$ related to precipitation and $\boldsymbol{E}_t$ associated with the seismic-velocity drop during the 2016 Kumamoto earthquake based on Wang et al. (2017), respectively. Because the explanatory variables are recognized as hyper-parameters in this study, they are deterministic at this level. Subsequently, they are estimated by Maximum Likelihood Method at the higher level (see section 5 for details). Section 5.3 also shows how to choose explanatory variables based on likelihood. $\boldsymbol{\epsilon}_t$ and $\boldsymbol{\eta}_t$ are mutually independent random variables, subject to normal distribution ($\mathcal{N}$) with zero means and covariance matrix $\boldsymbol{H}_t$ and $\boldsymbol{Q}_t$, respectively. The model $\boldsymbol{m}^p$ are defined by

$$\boldsymbol{m}^p(\boldsymbol{\alpha}_t + \boldsymbol{R}_t + \boldsymbol{E}_t) \equiv \begin{pmatrix} m^p(\boldsymbol{\alpha}_t + \boldsymbol{R}_t + \boldsymbol{E}_t; -\tau_e) \\ \vdots \\ m^p(\boldsymbol{\alpha}_t + \boldsymbol{R}_t + \boldsymbol{E}_t; -\tau_s) \\ m^p(\boldsymbol{\alpha}_t + \boldsymbol{R}_t + \boldsymbol{E}_t; \tau_s) \\ \vdots \\ m^p(\boldsymbol{\alpha}_t + \boldsymbol{R}_t + \boldsymbol{E}_t; \tau_e) \end{pmatrix}. \tag{7}$$

Since the sampling interval of CCFs is 0.4 s, the dimension of the vectors $\boldsymbol{y}_r^p$ and $\boldsymbol{m}^p$ is $2 \cdot ((\tau_e - \tau_s)/0.4 + 1) = 400$. With an assumption of the constant data covariance with respect to time and lag time, $\boldsymbol{H_t}$ can be written by a diagonal matrix:

$$\boldsymbol{H}_t \equiv h_0 \boldsymbol{I}, \tag{8}$$

where h_0 is a prior data covariance and $\boldsymbol{I}$ is the 400×400 identity matrix. Assuming that the amplitude A_t does not correlate with the seismic velocity change γ_t, we can write $\boldsymbol{Q}_t$ as a diagonal matrix:

$$\boldsymbol{Q}_t \equiv \begin{pmatrix} q_0 & 0 \\ 0 & q_1 \end{pmatrix}, \tag{9}$$

where q_0 and q_1 are a prior model covariance. h_0 is estimated from the time average of the squared difference between $\phi_t^p(\tau)$ and the reference $\varphi_{ref}^p(\tau)$. Since the amplitude A_t is a kind of normalization factor, it is difficult to separate the origins: volcanic, precipitation, or earthquake. For simplicity, we omitted the amplitude term A_t for precipitation and earthquakes. Accordingly $\boldsymbol{R}_t$ and $\boldsymbol{E}_t$ are given by,

$$\boldsymbol{R}_t \equiv \begin{pmatrix} 0 \\ r_t \end{pmatrix}, \boldsymbol{E}_t \equiv \begin{pmatrix} 0 \\ e_t \end{pmatrix}. \tag{10}$$

The state variable $\boldsymbol{\alpha}_t$ has an initial value $\boldsymbol{a}_1$ at $t = 1$ subject to a normal distribution $\sim N(\boldsymbol{a}_1, \boldsymbol{P}_1)$ defined by

$$\boldsymbol{a}_1 \equiv \begin{pmatrix} A_1 \\ \gamma_1 \end{pmatrix}, \boldsymbol{P}_1 \equiv \begin{pmatrix} p_0 & 0 \\ 0 & p_1 \end{pmatrix}, \tag{11}$$

where A_1 is a prior initial amplitude, γ_1 is a prior initial stretching factor, p_0 and p_1 are a prior model covariance for the initial value.

First, we assumed that $\boldsymbol{Q}_t$, $\boldsymbol{R}_t$, $\boldsymbol{E}_t$ and $\boldsymbol{P}_1$ are given in advance; that is, they are recognized as hyper-parameters. At the higher level, we estimated the hyper-parameters using the Maximum Likelihood Method as discussed in the next section.

We linearized equation (1) (e.g., Weaver et al., 2011) in order to apply the extended Kalman filter. We consider the update of state variable from the initial guess $\hat{\boldsymbol{\alpha}}_t \equiv (\hat{A}_t, \hat{\gamma}_t)^T$. Assuming that the increment from the initial guess $\Delta\boldsymbol{\alpha}$ is small, Taylor series of $\boldsymbol{m}^p$ in equation (5) at around the initial guess $\hat{\boldsymbol{\alpha}}_t$ up to 1st order lead the following equation,

$$\boldsymbol{m}^p(\hat{\boldsymbol{\alpha}}_t + \Delta\boldsymbol{\alpha} + \boldsymbol{R}_t + \boldsymbol{E}_t) = \boldsymbol{m}^p(\hat{\boldsymbol{\alpha}}_t + \boldsymbol{R}_t + \boldsymbol{E}_t) + \boldsymbol{\zeta}_t^p \Delta\boldsymbol{\alpha}, \tag{12}$$

where

$$\boldsymbol{\zeta}_t^p = \begin{pmatrix} \varphi_{ref}^p(-(1+\hat{\gamma}_t + r_t + e_t)\tau_e) & -\hat{A}_t\tau_e\dot{\varphi}_{ref}^p(-(1+\hat{\gamma}_t + r_t + e_t)\tau_e) \\ \vdots & \vdots \\ \varphi_{ref}^p(-(1+\hat{\gamma}_t + r_t + e_t)\tau_s) & -\hat{A}_t\tau_s\dot{\varphi}_{ref}^p(-(1+\hat{\gamma}_t + r_t + e_t)\tau_s) \\ \varphi_{ref}^p((1+\hat{\gamma}_t + r_t + e_t)\tau_s) & \hat{A}_t\tau_s\dot{\varphi}_{ref}^p((1+\hat{\gamma}_t + r_t + e_t)\tau_s) \\ \vdots & \vdots \\ \varphi_{ref}^p((1+\hat{\gamma}_t + r_t + e_t)\tau_e) & \hat{A}_t\tau_e\dot{\varphi}_{ref}^p((1+\hat{\gamma}_t + r_t + e_t)\tau_e) \end{pmatrix}, \tag{13}$$

and $\dot{\varphi}$ represents the derivative of φ.

Since nine components of the cross-correlation functions were used in this study, we define the following vectors:

$$\boldsymbol{Y}_t \equiv \begin{pmatrix} \boldsymbol{y}_t^{RR} \\ \boldsymbol{y}_t^{RT} \\ \boldsymbol{y}_t^{RZ} \\ \boldsymbol{y}_t^{TR} \\ \boldsymbol{y}_t^{TT} \\ \boldsymbol{y}_t^{TZ} \\ \boldsymbol{y}_t^{ZR} \\ \boldsymbol{y}_t^{ZT} \\ \boldsymbol{y}_t^{ZZ} \end{pmatrix}, \boldsymbol{Z}_t(\hat{\boldsymbol{\alpha}}_t) \equiv \begin{pmatrix} \boldsymbol{\zeta}_t^{RR} \\ \boldsymbol{\zeta}_t^{RT} \\ \boldsymbol{\zeta}_t^{RZ} \\ \boldsymbol{\zeta}_t^{TR} \\ \boldsymbol{\zeta}_t^{TT} \\ \boldsymbol{\zeta}_t^{TZ} \\ \boldsymbol{\zeta}_t^{ZR} \\ \boldsymbol{\zeta}_t^{ZT} \\ \boldsymbol{\zeta}_t^{ZZ} \end{pmatrix}, \boldsymbol{M}_t(\hat{\boldsymbol{\alpha}}_t) \equiv \begin{pmatrix} \boldsymbol{m}^{RR}(\hat{\boldsymbol{\alpha}}_t + \boldsymbol{R}_t + \boldsymbol{E}_t) \\ \boldsymbol{m}^{RT}(\hat{\boldsymbol{\alpha}}_t + \boldsymbol{R}_t + \boldsymbol{E}_t) \\ \boldsymbol{m}^{RZ}(\hat{\boldsymbol{\alpha}}_t + \boldsymbol{R}_t + \boldsymbol{E}_t) \\ \boldsymbol{m}^{TR}(\hat{\boldsymbol{\alpha}}_t + \boldsymbol{R}_t + \boldsymbol{E}_t) \\ \boldsymbol{m}^{TT}(\hat{\boldsymbol{\alpha}}_t + \boldsymbol{R}_t + \boldsymbol{E}_t) \\ \boldsymbol{m}^{TZ}(\hat{\boldsymbol{\alpha}}_t + \boldsymbol{R}_t + \boldsymbol{E}_t) \\ \boldsymbol{m}^{ZR}(\hat{\boldsymbol{\alpha}}_t + \boldsymbol{R}_t + \boldsymbol{E}_t) \\ \boldsymbol{m}^{ZT}(\hat{\boldsymbol{\alpha}}_t + \boldsymbol{R}_t + \boldsymbol{E}_t) \\ \boldsymbol{m}^{ZZ}(\hat{\boldsymbol{\alpha}}_t + \boldsymbol{R}_t + \boldsymbol{E}_t) \end{pmatrix} \tag{14}$$

4.1 Calculation of the reference CCF

First, we estimated the preliminary reference CCF φ_{ref}^p for the pth component pair as,

$$\varphi_{ref}^p(\tau) = \frac{1}{n}\sum_{t=1}^{n} \phi_t^p(\tau). \tag{15}$$

With the preliminary reference CCF, preliminary $\hat{\gamma}_t$ was measured using an extended Kalman filter/smoother described in the following subsections. Then we recalculated the reference as

$$\varphi^p_{ref}(\tau) = \frac{1}{n}\sum_{t=1}^{n} \phi^p_t(\tau(1+\hat{\gamma}_t)). \tag{16}$$

After recalculating $\hat{\gamma}_t$ with the revised reference, we measured the temporal variations that are discussed herein.

4.2 Extended Kalman filter

The state vector $\boldsymbol{\alpha}_t$ was estimated by the recursive linear Kalman (forward) filter and (backward) smoother. The Kalman filter/smoother is a powerful solver of a state-space model, which obeys Gaussian distributions (e.g., Durbin & Koopman, 2012). The method has been applied for many geophysical problems (e.g. geodetic inversions, Segall & Matthews, 1997; Aoki et al., 1999), and recursive travel-time inversion in seismology (Ogiso et al., 2005). Since state vectors obey a normal distribution, the means and the covariance matrices characterized the statistics of the vector completely. Let us consider the conditional mean and covariance matrix of the state variables at time $t = 2 \cdots n$ for given data through $\boldsymbol{Y}_1, \cdots, \boldsymbol{Y}_{t-1}$ as,

$$\hat{\boldsymbol{\alpha}}_{t|t-1} \equiv E(\alpha_t \mid \boldsymbol{Y}_1, \cdots, \boldsymbol{Y}_{t-1}) \tag{17}$$

$$\hat{\boldsymbol{P}}_{t|t-1} \equiv Cov(\alpha_t \mid \boldsymbol{Y}_1, \cdots, \boldsymbol{Y}_{t-1}), \tag{18}$$

where n is number of the data, $E()$ represents expectation, and $Cov()$ represents covariance. $\hat{\boldsymbol{\alpha}}_{t|t-1}$ is also known as the one-step ahead predictor (Durbin & Koopman, 2012). Since no data can constrain $\hat{\boldsymbol{\alpha}}_{1|0}$ and $\hat{\boldsymbol{P}}_{1|0}$, they are given by the initial values: $\hat{\boldsymbol{\alpha}}_{1|0} = \boldsymbol{a}_1$ and $\hat{\boldsymbol{P}}_{1|0} = \boldsymbol{P}_1$.

These are updated from the initial value $\boldsymbol{a}_1$ and $\boldsymbol{P}_1$ using the following equation:

$$\hat{\boldsymbol{\alpha}}_{t+1|t} = \hat{\boldsymbol{\alpha}}_{t|t-1} + \boldsymbol{K}_t \boldsymbol{v}_t \tag{19}$$

$$\hat{\boldsymbol{P}}_{t+1|t} = \hat{\boldsymbol{P}}_{t|t-1} - \boldsymbol{K}_t(\boldsymbol{Z}_t \hat{\boldsymbol{P}}_{t|t-1} \boldsymbol{Z}_t^T + \boldsymbol{H}_t)\boldsymbol{K}_t^T + \boldsymbol{Q}_t, \tag{20}$$

where Kalman gain $\boldsymbol{K}_t$ is given by

$$\boldsymbol{K}_t = \hat{\boldsymbol{P}}_{t|t-1} \boldsymbol{Z}_t^T (\boldsymbol{H}_t + \boldsymbol{Z}_t \hat{\boldsymbol{P}}_{t|t-1} \boldsymbol{Z}_t^T)^{-1}, \tag{21}$$

and the innovation vector $\boldsymbol{v}_t$ is given by

$$\boldsymbol{v}_t = \boldsymbol{Y}_t - \boldsymbol{M}_t(\hat{\boldsymbol{\alpha}}_{t|t-1}). \tag{22}$$

Since the number of model parameters of 2 is much smaller than length of $\boldsymbol{Y}_t$ of 36000 (9 components $\times$ 400 points), the matrix calculation of equation (21) can be reduced using the following matrix inversion lemma (Tarantola & Valette, 1982; Ogiso et al., 2005),

$$(\boldsymbol{H}_t + \boldsymbol{Z}_t \hat{\boldsymbol{P}}_{t|t-1} \boldsymbol{Z}_t^T)^{-1} = \boldsymbol{H}_t^{-1} - \boldsymbol{H}_t^{-1} \boldsymbol{Z}_t (\hat{\boldsymbol{P}}_{t|t-1}^{-1} + \boldsymbol{Z}_t^T \boldsymbol{H}_t^{-1} \boldsymbol{Z}_t)^{-1} \boldsymbol{Z}_t^T \boldsymbol{H}_t^{-1}. \tag{23}$$

Here we assumed that the errors of the CCF are independent of lag time, and the variances were the same throughout the lag time. Since we assumed that the covariance matrix of data error $\boldsymbol{H}_t$ is represented by $\boldsymbol{H}_t = h_0 \boldsymbol{I}$ (equation (8)), the forward recursive equations (19) and (20) could be simplified as,

$$\hat{\boldsymbol{\alpha}}_{t+1|t} = \hat{\boldsymbol{\alpha}}_{t|t-1} + \boldsymbol{\Xi}_t \boldsymbol{\Gamma}_t \tag{24}$$

$$\hat{\boldsymbol{P}}_{t+1|t} = \hat{\boldsymbol{P}}_{t|t-1} - \boldsymbol{\Xi}_t(\boldsymbol{S}_t \hat{\boldsymbol{P}}_{t|t-1} \boldsymbol{S}_t + h_0 \boldsymbol{S}_t)\boldsymbol{\Xi}_t^T + \boldsymbol{Q}_t, \tag{25}$$

where $\boldsymbol{S}_t$ and $\boldsymbol{\Xi}_t$ are 2×2 matrices as:

$$\boldsymbol{S}_t \equiv \sum_p (\boldsymbol{\zeta}_t^p)^T \boldsymbol{\zeta}_t^p, \tag{26}$$

$$\boldsymbol{\Gamma}_t \equiv \sum_p (\boldsymbol{\zeta}_t^p)^T \boldsymbol{v}_t^p, \tag{27}$$

$$\boldsymbol{\Xi}_t \equiv \left(\frac{1}{h_0} \hat{\boldsymbol{P}}_{t|t-1} - \frac{1}{h_0^2} \hat{\boldsymbol{P}}_{t|t-1} \boldsymbol{S}_t \left(\frac{\boldsymbol{S}_t}{h_0} + \hat{\boldsymbol{P}}_{t|t-1}^{-1} \right)^{-1} \right). \tag{28}$$

4.3 Kalman smoother

Next, let us consider the conditional mean $\hat{\boldsymbol{\alpha}}_{t|n}$ and conditional covariance matrix $\hat{\boldsymbol{P}}_{t|n}$ of the state variables at time t for all data through $\boldsymbol{Y}_1, \cdots, \boldsymbol{Y}_n$. With the $\hat{\boldsymbol{\alpha}}_{t|t-1}$ and $\hat{\boldsymbol{P}}_{t|t-1}$ $(t = 2, \cdots, n)$ estimated in the previous subsection, they can be calculated by the following backward recursive equations,

$$\hat{\boldsymbol{\alpha}}_{t|n} = \hat{\boldsymbol{\alpha}}_{t|t-1} + \hat{\boldsymbol{A}}_t (\hat{\boldsymbol{\alpha}}_{t+1|n} - \hat{\boldsymbol{\alpha}}_{t|t-1}), \tag{29}$$

$$\hat{\boldsymbol{P}}_{t|n} = \hat{\boldsymbol{P}}_{t+1|t} - \boldsymbol{Q}_t + \hat{\boldsymbol{A}}_t (\hat{\boldsymbol{P}}_{t+1|n} - \hat{\boldsymbol{P}}_{t+1|t}) \hat{\boldsymbol{A}}_t^T. \tag{30}$$

where A_t is defined by

$$\hat{\boldsymbol{A}}_t = \left(\boldsymbol{I} - \boldsymbol{Q}_t \hat{\boldsymbol{P}}_{t+1|t}^{-1} \right), \tag{31}$$

The recursive equations were applied successively backward as $t = n-1, \cdots, 1$.

4.4 Temporal change of seismic wave velocity

First, we tentatively estimated the temporal variations without the explanatory variables. For given hyper-parameters $r_t = e_t = 0$, $p_0 = 5 \times 10^{-4}$, $p_1 = 5 \times 10^{-5}$, we estimated the state variables using the extended Kalman filter/smoother. Figure 4 shows the result of temporal variations in seismic velocity $\hat{\gamma}_{t|n}$ and the corresponding standard deviation by applying CCFs of the station pair between TKW and TKS. The figure shows clear seasonal variation, and the velocity drops coincide with strong rainfalls (blue bars in the figure). The red line shows the precipitation model (see the next section for details). This figure also shows a sudden velocity drop of about 0.1 % when the Kumamoto earthquake occurred in 2016. To detect signals associated with volcanic eruptions, we subtracted the precipitation effects and the earthquake drop from the temporal variations in seismic velocity. For the subtraction, we infer the hyper-parameters, which represent the model covariances, precipitation effects, and earthquake, drop by the Maximum Likelihood method in the next section.

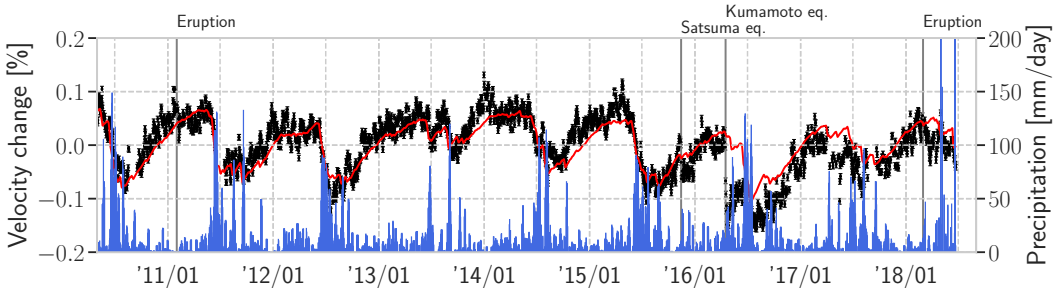

Figure 4. Row temporal changes of the pair between TKW and TKS with the prediction from the precipitation. The red line shows prediction by the precipitation model ($\tau_g = 195$ days, and $A_g = -6.84 \times 10^{-2}$ [%/m]), as described in the next section.

5 Maximum Likelihood Method for determining the hyper-parameters

In the previous section, we applied the extended Kalman filter/smoother, assuming that the hyper-parameters were given at the lower level. This section shows how to infer the hyper-parameters using the Maximum Likelihood Method at the higher level of this technique.

The logarithmic likelihood $\ln L$ is given (e.g., Segall & Matthews, 1997; Durbin & Koopman, 2012) by

$$\ln L = -\frac{nN}{2}\ln 2\pi - \frac{1}{2}\sum_{t=1}^{n}\left(\ln(\det(\boldsymbol{F}_t)) + \hat{\boldsymbol{d}}_{t|t-1}\right), \tag{32}$$

where $\boldsymbol{F}_t$ and $\hat{\boldsymbol{d}}_{t|t-1}$ are given by,

$$\boldsymbol{F}_t \equiv h_0\boldsymbol{I} + \boldsymbol{Z}_t\hat{\boldsymbol{P}}_{t|t-1}\boldsymbol{Z}_t^T, \tag{33}$$

and

$$\hat{\boldsymbol{d}}_{t|t-1} = \frac{1}{h_0^2}\left(h_0\boldsymbol{v}_t^T\boldsymbol{v}_t - \boldsymbol{\Gamma}_t^T\left(\hat{\boldsymbol{P}}_{t|t-1}^{-1} + \frac{\boldsymbol{S}_t}{h_0}\right)^{-1}\right)\boldsymbol{\Gamma}_t, \tag{34}$$

respectively. We maximized the logarithmic likelihood $\ln L$ with respect to the hyper-parameters.

First, we describe how to model the hyper-parameters for explaining the precipitation effects and the reduction associated with the 2016 Kumamoto earthquake in the following two subsections.

5.1 A model for the precipitation effects

Many researchers have reported periodic changes in seismic wave velocity associated with external sources such as tides (e.g., Yamamura et al., 2003; Takano et al., 2014, 2019), thermoelastic effects (e.g., Hillers, Ben-Zion, et al., 2015; Wang et al., 2017), and snow loading (e.g., Wang et al., 2017). The correspondence between strong rainfall and the seismic velocity changes shown in Figure 4 suggests the dominance of the precipitation effect in this case. For modeling temporal changes of seismic wave velocity caused by precipitation, we considered two models: the model based on diffusion of a pore pressure (Talwani et al., 2007; Rivet et al., 2015; Lecocq et al., 2017; Wang et al., 2017), and the hydrological model (Sens-Schönfelder & Wegler, 2006).

The first model considered diffusion of pore pressure in a poroelastic medium with a spatial scale of several km, which induces seismic velocity changes. This model also required the sensitivity of seismic velocity to changes in pore pressure. As discussed in section 7.2, the sensitivity is an order of magnitude smaller than the typical values. The diffusion of pore pressure also caused significant time delay, which is not consistent with the observations in this study.

The second model related the seismic velocity to the groundwater level at a shallow depth due to the precipitation (Sens-Schönfelder & Wegler, 2006). Since the groundwater level reaches a shallow depth of about 100 m in this region (Kagiyama et al., 1996; Tsukamoto et al., 2018), we regarded the second model more relevant. The response of the groundwater level to the precipitation is given by an exponential function (Sens-Schönfelder & Wegler, 2006; Kim & Lekic, 2019). The amount of ground water storage g_t is given by

$$g_t = \int_t^\infty \left(p(\tau) - \langle p\rangle\right) e^{-\frac{t-(\tau+\delta)}{\tau_g}} d\tau, \tag{35}$$

where p is daily precipitation, δ shows delay time, τ_g is the parameter describing the decay, $\langle p\rangle$ is the average precipitation throughout the analyzed time period. We modeled

that the explanatory variable for precipitation r_t is proportional to g_t as,

$$r_t = A_g g_t = A_g \int_t^\infty \left(p(\tau) - \langle p \rangle\right) e^{-\frac{t-(\tau+\delta)}{\tau_g}} d\tau, \tag{36}$$

where A_g is the sensitivity of seismic wave velocity to the ground water level. Since there exists ambiguity of the modeling, A_g, τ_g, and δ should be constrained by the observations practically. We regard A_g, τ_g and δ as hyper-parameters, and infer their values by the Maximum Likelihood Method as shown later in this section.

To validate the second model quantitatively, we estimate the sensitivity A_g based on a physical model: density perturbation due to groundwater levels causes the temporal change associated with precipitation. Since surface waves are dominant in the wavefield in this frequency range, the depth sensitivity can be represented by that of the surface waves for a 1-D medium (Obermann et al., 2013). We consider only Rayleigh waves for simplicity, since a similar discussion can be applicable for Love waves. The phase velocity perturbation of Rayleigh waves δc can be related to perturbations of density ρ, bulk modulus κ, andrigidity μ using the partial derivatives of phase velocity (Takeuchi & Saito, 1972) as,

$$\frac{\delta c}{c} = \int \left(K_\rho(z) \frac{\delta \rho(z)}{\rho(z)} + K_\kappa(z) \frac{\delta \kappa(z)}{\kappa(z)} + K_\mu(z) \frac{\delta \mu(z)}{\mu(z)} \right) dz, \tag{37}$$

where c is the phase velocity, and K_ρ, K_κ and K_μ are the Fréchet derivatives relating the fractional perturbation of phase velocity $\delta c/c$ to the fractional perturbations $\delta\rho/\rho$, $\delta\kappa/\kappa$, $\delta\mu/\mu$. The Fréchet derivatives are also known as the depth sensitivity kernels. Figure 5 shows an example of a depth sensitivity kernel at 0.6 Hz for the density and S-wave velocity models shown in the figure.

Working under the two assumption of (i) no temporal changes in bulk modulus κ and the rigidity μ, and (ii) the groundwater level of about 100 m, the temporal change r_t can be estimated as,

$$r_t = \int K_\rho(z) \frac{\delta \rho(z)}{\rho(z)} dz \approx K_\rho(0) \frac{\rho_w g_t}{\rho(0)}, \tag{38}$$

where ρ_w is water density. Accordingly, A_g can be written by $K_\rho(0)\frac{\rho_w}{\rho(0)}$. For example, with the model shown by Figure 5, A_g is estimated to be -7.5×10^{-2} [%/m]. The consistency between this estimate of -7.5×10^{-2} [%/m] and the fitting result of -6.84×10^{-2} [%/m] supports our model.

For estimation of the hyper-parameters, initial values are required. We estimated them in two steps. First, using the preliminary reference CCF, $\hat{\gamma}_{t|n}$ was calculated for each station pair. In equation (5), $\boldsymbol{R}_t$ is assumed to be $\mathbf{0}$. Then, A_g and τ_g were estimated by calculating the least squared difference between r_t and $\hat{\gamma}_{t|n}$. δ is fixed to 0. The red line in Figure 4 shows the initial estimate of a pair between TKW and TKS: $\tau_g =$ 195 days and $A_g = -6.84 \times 10^2$ [%/m]. This figure shows that the empirical model can predict the seasonal variations well. To avoid the effects of the sudden drop due to the 2016 Kumamoto earthquake, we used the data from before the earthquake in the estimation.

5.2 A model for the drops associated with 2016 Kumamoto earthquake

After the reduction of the effect of precipitation with the tentative hyper-parameters, the resultant temporal change shows sudden drops of seismic wave velocity associated with the 2016 Kumamoto earthquake (Figure 6). Since the drop related to the Kumamoto earthquake reaches 0.1 %, we modeled it by an exponential decay (Hobiger et al., 2016; Gassenmeier et al., 2016; Sens-Schönfelder & Eulenfeld, 2019) as,

$$e_t = A_t e^{\frac{t-t_0}{\tau_e}}, \tag{39}$$

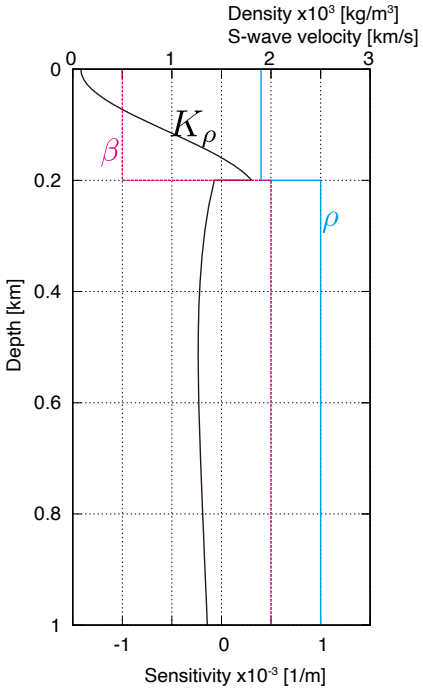

Figure 5. Depth sensitivity kernel to density perturbations at 0.6 Hz. The density ρ and the S-wave velocity β are plotted. P-wave velocities are 1.91 km/s from 0 to 0.2 km, and 4 km/s below 0.2 km.

where A_t is amplitude of the drop, t_0 is the origin time of the Kumamoto earthquake, and τ_e is the decay time. We omitted a term of non-recovering coseismic velocity drops (Hobiger et al., 2016) as the term could not be detected, as shown later (see Figure 10).

5.3 Estimation of the hyper-parameters by Maximum Likelihood Method

To reduce the number of hyper-parameters, we assumed that the expected value of the initial state variable $\boldsymbol{a}_1$ is given by $(1, \gamma_1)$, and the covariance matrix $\boldsymbol{P}_1$ is equal to $\boldsymbol{Q}_t$.

$\ln L$ is a function of hyper-parameters $\boldsymbol{\beta}$, where

$$\boldsymbol{\beta} = (p_0, p_1, \tau_g, A_g, \delta, \gamma_1, A_e, \tau_e). \tag{40}$$

The logarithmic likelihood $\ln L$ was maximized with respect to the hyper-parameters using a quasi-Newton method L-BFGS-B, which is a limited memory algorithm for solving large nonlinear optimization problems subject to simple bounds on the variables (Zhu et al., 1994; Durbin & Koopman, 2012).

Figure 7 shows estimated hyper-parameters, which are well constrained by the observations. Figure 7 (a) shows the model standard deviations of amplitude A_t of about 5×10^3% and those of stretching factor γ_t of about 0.1%. We note that the observed data constrain the model standard deviations. Figure 7 (b) shows a trend of decreasing sensitivity A_g with decreasing decay time τ_g. This result suggests that the groundwater level changes at shallower depths have shorter time decay time τ_g, because the depth sensitivity kernel is negative and decreases to the ground surface (Figure 5). Figure 7 (c), which compares A_e and τ_e, shows the drop when the earthquake becomes larger, de-

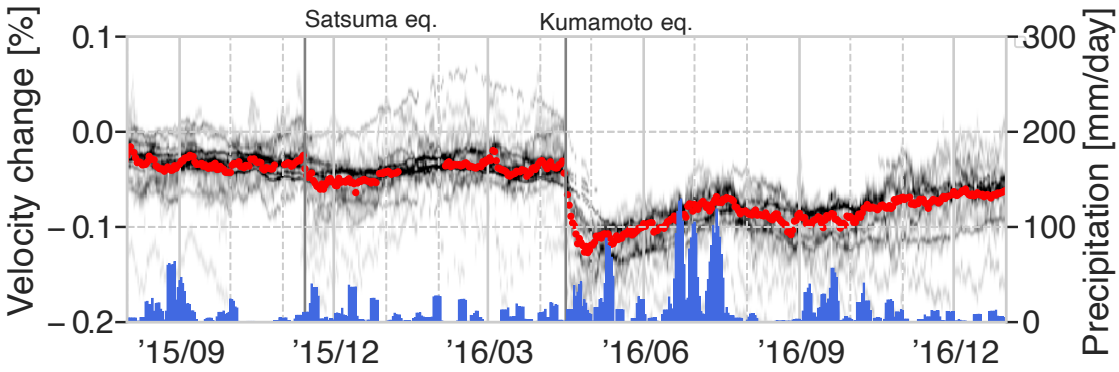

Figure 6. Velocity change associated with the 2016 Kumamoto earthquake. The seismic velocity drop when the earthquake occurred, and recovered over a time scale of three months. The grayscale shows marginal probability with all CCFs (see next section for details). The red dots show a median of all the measurements. The red dots also show a minor drop during the 2015 Satsuma earthquake.

443 creasing the recovery time. This result suggests that the stronger drop and shorter re-
444 covery occurred at shallower depths.

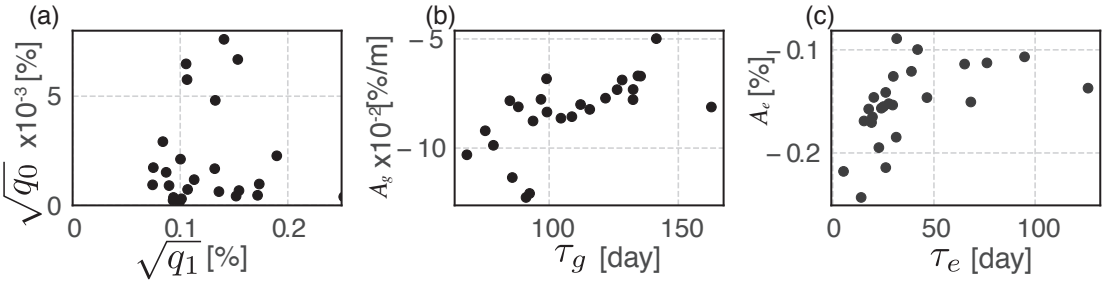

Figure 7. Estimated hyper-parameters. (a) scatter plot against standard deviations of the model: $\sqrt{q_0}$ and $\sqrt{q_1}$, (b) scatter plot against hyper-parameters of precipitation effects: τ_g and A_g, (c) scatter plot against hyper-parameters of the drop during the Kumamoto earthquake: A_e and τ_e.

445 To determine how well the observations constrain the hyper-parameters $\boldsymbol{\beta}$, we es-
446 timated the sensitivity of the logarithmic likelihood of the perturbations around the op-
447 timal value $\boldsymbol{\beta}^{opt}$. Figure 8 shows an increment of logarithmic likelihood to the optimal
448 value of $\Delta \ln L$ as a function of a hyper-parameter. We perturbed each hyper-parameter
449 within 50%, fixing all other hyper-parameters to the optimal values. Within this hyper-
450 parameter range, the minima of $\Delta \ln L$ for all the hyper-parameters were smaller than
451 -1.

452 Here we considered the appropriate number of hyper-parameters using the Akaike
453 Information Criterion (AIC, Akaike, 1974) defined by

$$AIC_K = -2 \ln \hat{L}_K + 2K, \tag{41}$$

455 where K is the number of hyper-parameters, and $\ln \hat{L}_K$ represents the maximum like-
456 lihood for the K hyper-parameters. We choose the hyper-parameter if AIC_K decreases

with the addition of a new hyper-parameter: i.e. the increment $\Delta AIC \equiv AIC_K - AIC_{K-1}$ is smaller than 0. Assuming that $\ln \hat{L}_{K-1} - \ln \hat{L}_K$ can be approximated by $\Delta \ln L$ shown in Figure 8, the ΔAIC is written by $2(\Delta \ln L + 1)$. The addition of a hyper-parameter is appropriate if $\Delta \ln L < -1$. Assuming that the ambiguity of each parameter is about 50%, for example, β_i is fixed at $0.5\beta_i^{opt}$ as the prior value. Since all the $\Delta \ln L$ at $\beta_i/\beta_i^{opt} = 0.5$ in Figure 8 are smaller than -1, all the hyper-parameters used meet this condition. This choice of hyper-parameters also makes the iterations of the L-BFGS-B method stable.

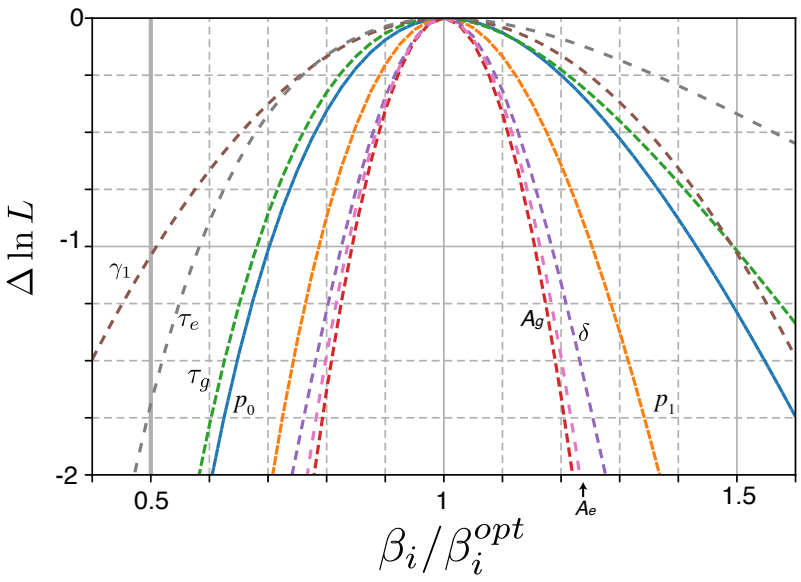

Figure 8. Logarithmic likelihood as a function of the normalized hyper-parameters. The horizontal axis shows relative value of hyper-parameters, and the vertical axis shows increments of logarithmic likelihood to the optimal value $\ln L(\boldsymbol{\beta}^{opt})$. The corresponding hyper-parameters (β_i) are also shown in this figure.

6 Temporal changes of seismic wave velocity

Using the inferred hyper-parameters, we estimated state variables for all pairs of stations. Red lines in the upper triangular portion of Figure 9 show the total temporal changes of seismic wave velocity $\hat{\gamma}_{t|n} + r_t + e_t$. The blue lines show only the explanatory variables $r_t + e_t$ for precipitation and the earthquake. The explanatory variables can explain majority of the aspects of the estimated temporal changes.

The lower triangular portion of Figure 9 shows the resultant $\hat{\boldsymbol{\alpha}}_{t|n}$. The blue lines show the amplitude $\hat{A}_{t|n}$, which show the local minimum in 2015. High activities of low-frequency volcanic tremor at Mt. Aso (Figure 1) could distort the coherency (Kaneshima et al., 1996; Hendriyana & Tsuji, 2019; Sandanbata et al., 2015). The red lines show seismic velocity changes, $\hat{\gamma}_{t|n}$, after the subtraction of the explanatory variables. They show a consistent long term variation with a time scale of about five years with an amplitude of about 0.05 %. Although most station pairs do not show significant temporal changes associated with the 2011 eruption, the pair between SMW and SMN shows a significant drop in 2011. The upper triangular portion shows the precipitation effect and the drop associated with the earthquake are well subtracted using the explanatory variables.

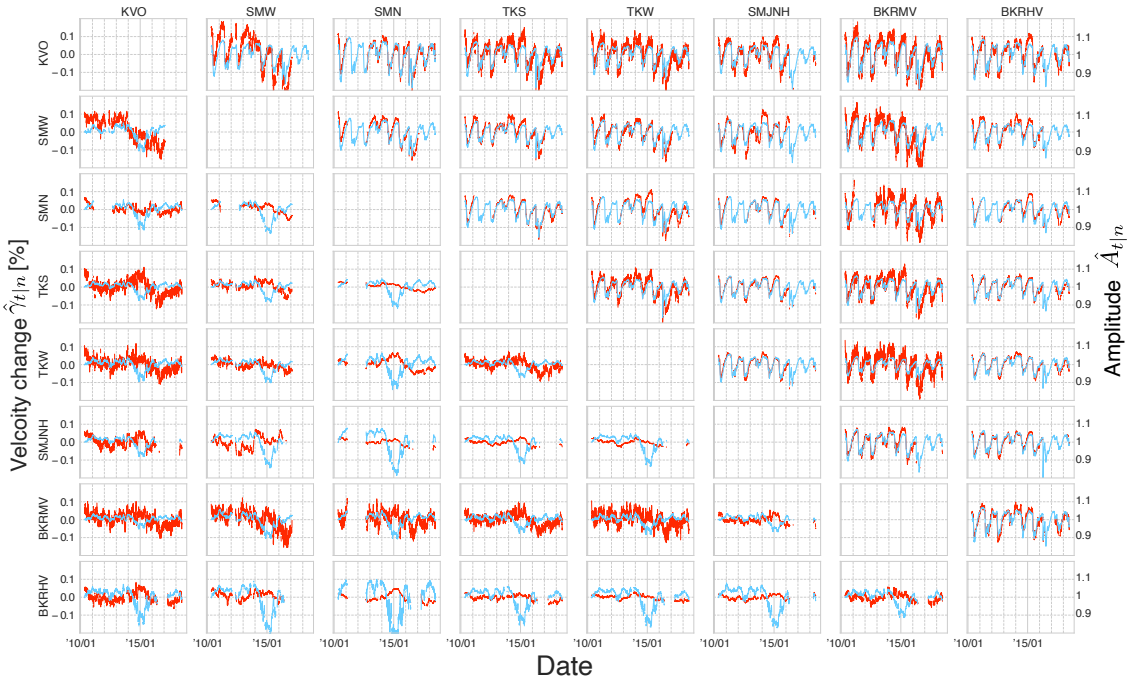

Figure 9. The lower triangular portion: resultant $\hat{\boldsymbol{\alpha}}_{t|n}$. The red lines show seismic velocity change $\hat{\gamma}_{t|n}$ within 0.1%. The blued lines show the amplitude perturbations $\hat{A}_{t|n}$, which show a local minimum in 2015. The upper triangular portion: Blue lines show estimated seismic velocity changes $r_t \quad + \quad e_t$, which explain the precipitation effect and the drop during the Kumamoto earthquake, whereas red ones show estimated whole seismic velocity changes $\hat{\gamma}_{t|n} + r_t + e_t$.

To discuss the long-term variations, we considered the marginal probability density with all pairs of stations. Figure 10(a) shows the marginal probability density over 8 years with an assumption that each measurement is independent. The probability density $f_t(\gamma)$ as a function of seismic velocity change γ is defined by

$$f_t(\gamma) \equiv \frac{1}{28} \sum_{j=1}^{28} \mathcal{N}({}^j\hat{\gamma}_{t|n}, {}^j\hat{q}_{t|n}), \tag{42}$$

where $\mathcal{N}$ represents normal distribution, ${}^j\hat{\gamma}_{t|n}$ is the conditional mean of seismic velocity changes, ${}^j\hat{q}_{t|n}$ is the corresponding conditional covariance, j indicates a station pair, and 28 is the total number of station pairs. The marginal probability density (Figure 10(a)) shows no significant changes associated with the 2011 and 2018 eruptions of Shinmoe-dake. However, areal strain calculated from GNSS observation shows inflation and deflation due to changes in the magma reservoir during the 2011 eruption, and the 2018 eruption (Nakao et al., 2013; Kozono et al., 2013; Yamada et al., 2019) (Figure 10(b)). The areal strain also shows the static change due to the 2016 Kumamoto earthquake, whereas $f_t(\gamma)$ does not show significant static change.

Apart from jumps of the areal strain associated with the eruptions and the earthquake, both the seismic velocity changes and the areal strain (Figure 10) show temporal variations with a time scale of about one year with local maxima in January 2012 and January 2013. After 2014, such temporal variations are no longer observed for both. One possible origin of the variations is the long term variations in groundwater levels (e.g., Lecocq et al., 2017). When modeling groundwater level in equation (35), we assumed constant drainage. Nevertheless, under realistic conditions, the drainage may change with time. Since the areal strain also shows a similar undulation pattern from 2010 to 2013, such a long-term variation may cause large scale deformations. The induced pore pressure change (Talwani et al., 2007) at deeper depth, on the order of km, could also cause seismic velocity changes (Wang et al., 2017; Rivet et al., 2015). In this study, however, the hydrological data were insufficient to verify this hypothesis.

7 Discussions

In the following subsections, we discuss two specific events: the drop of seismic wave velocity associated with the Kumamoto earthquake and the 2011 Shinmoe-dake eruption. Based on the observed features, we discuss the magma pathway beneath Shinmoe-dake.

7.1 The drop of seismic wave velocity after the Kumamoto earthquake

Our results show a sudden drop during the Kumamoto earthquake followed by a recovery from 10 to 100 days (Figure 7). Since the probability density $f_t(\gamma)$ does not show non-recovering coseismic velocity drops due to the static areal-strain change (Figure 10), the observed static strain change could not be the dominant source. Near-surface damage beyond the linear elastic regime could be a possible origin. For the discussion, we compare the susceptibility, which is defined by the ratio between observed reductions in seismic velocity and the estimated dynamic stress with that of the 2011 Tohoku earthquake (Brenguier et al., 2014).

We estimated the dynamic stress from the observed peak ground velocity (PGV) (Gomberg & Agnew, 1996). PGV in this region was about 5 cm/s during the Kumamoto earthquake, which was averaged over 3 components of PGV measured by the K-net, strong-motion seismograph network. The dynamic stress $\Delta\sigma \approx \mu v/c$ was estimated to be 0.5 MPa, where μ is the mean crustal shear modulus ($\sim$ 30 GPa), v is PGV, and c is the mean wave phase velocity of the Rayleigh wave ($\sim$ 3 km/s) (Brenguier et al., 2014). The susceptibility (Brenguier et al., 2014), which is defined by the ratio between observed re-

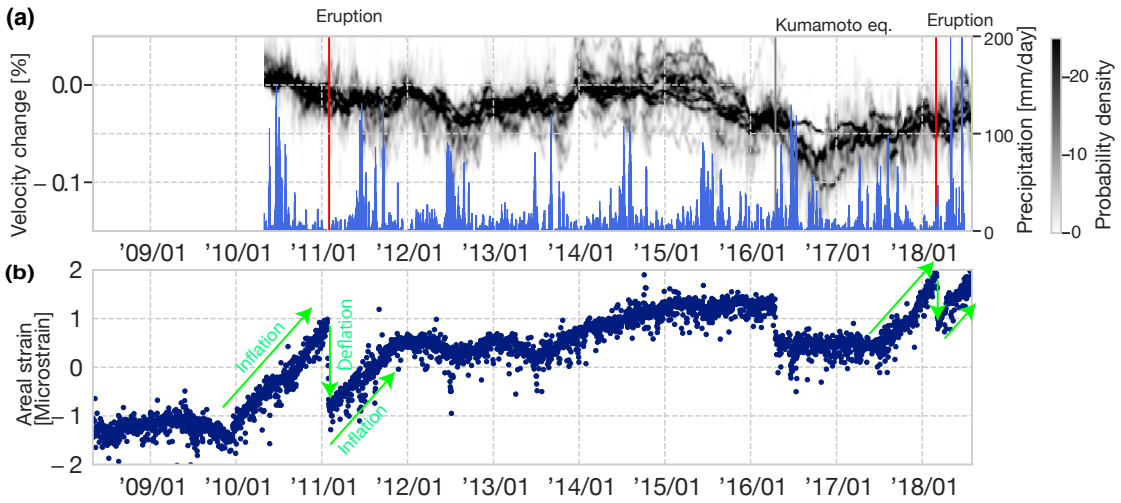

Figure 10. (a) Marginal probability density of all pairs of stations. The blue bars show daily precipitation data at the JMA meteorological station. The estimated seismic velocities scatter from Oct. 2014 to May 2015 when the activity of low frequency tremor at Mt. Aso occurs. (b) Areal strain calculated from three GEONET stations: Ebino, Miyakonojou2 and Makizono shown in Figure 1.

ductions in seismic velocity $\Delta c/c$ ($\sim 2\times10^{-3}$) and the estimated dynamic stress 0.5 MPa, was about 4×10^{-3} MPa^{-1}. This value is larger than susceptibility in the Mt. Fuji area and along the Tohoku volcanic during the Tohoku earthquake, whose value is about 1.5×10^{-3} MPa^{-1} (Brenguier et al., 2014). This observation suggests that the pressurized geofluid in the upper crust and/or near-surface is a possible origin for the seismic velocity changes.

We discuss the mechanism of the observed seismic velocity change as caused by the pressurized fluid. The exponential decay time scales ranged from 10 to 100 days, suggesting the lack of a relaxation process longer than 100 days (Snieder et al., 2017). The estimation of relatively short time scales dismisses the mechanisms of post-seismic relaxation of stress (e.g., Brenguier, Shapiro, et al., 2008) and diffusion of geofluid in the crust (Wang et al., 2019). The absence of non-recovering coseismic velocity drop during the 2016 Kumamoto earthquake suggests that the pressurization of geofluid in the linear elastic regime is unlikely to be the origin. This hypothesis is also consistent with the observation that the 2011 Tohoku earthquake did not trigger any volcanic and seismic activities in this region (Miyazawa, 2011). Near-surface damage due to the strong ground motions beyond the linear elastic regime, where rich groundwater exists, could be a plausible origin.

7.2 Temporal changes during the volcanic eruptions in 2011

The probability density of all the station pairs f_t (Figure 10(a)) does not show any temporal change associated with the volcanic eruptions from January 2011 to February 2011. However, geodetic observation showed the gradual magma intrusion over the time scale of a year and the discharge during the eruption (see the areal strain in Figure 10(b)). The geodetic source was located 5 km to the northwest of the summit at a depth of about 8 km (Nakao et al., 2013). Although the volumetric change caused enough strain (about

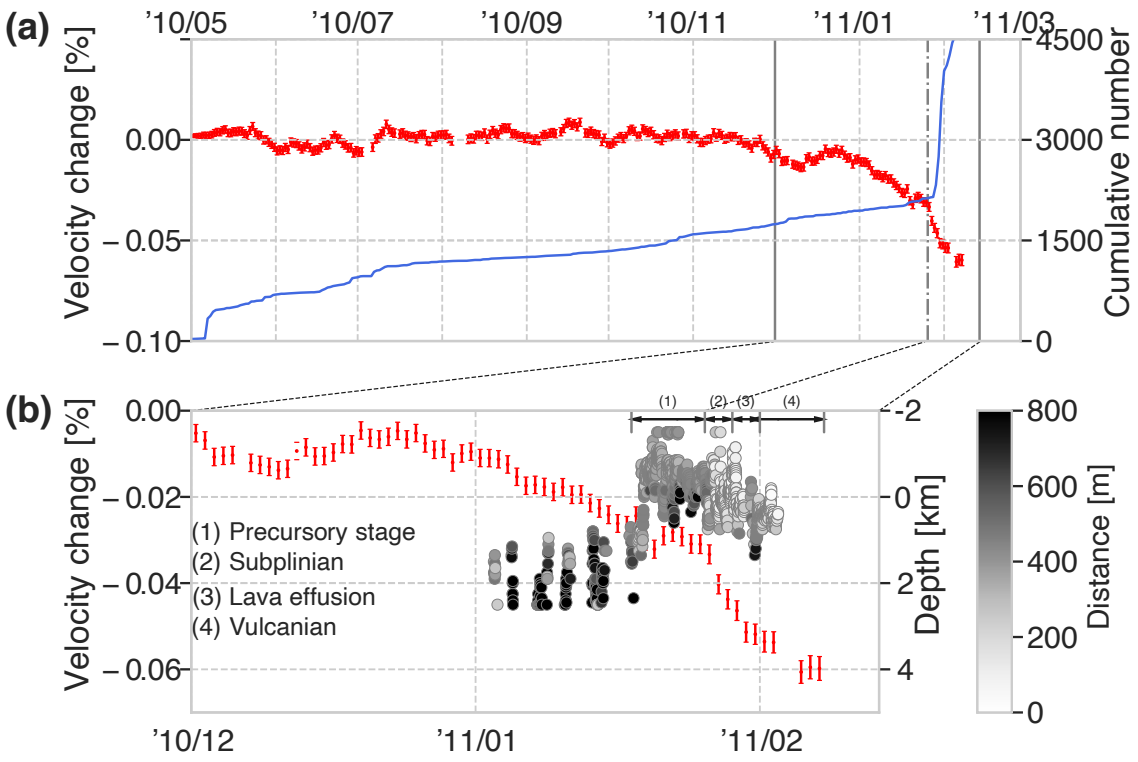

Figure 11. (a) Seismic velocity changes $\hat{\gamma}_{t_n}$ for the pair between SMN and SMW shown by red bars. The station SMN was damaged during the eruption. The line in sky blue shows the cumulative number of volcanic earthquakes determined by JMA below Shinmoe-dake. (b) Enlarged figure from October 1st, 2010 to February 14th, 2011. The panel also shows the depth of volcanic tremor (Ichihara & Matsumoto, 2017). The color of a circle shows the horizontal distance from the center of the summit to the hypocenter. Four periods: (1) Precursory stage, (2) Sub-Plinian, (3) Lava effusion, and (4) Vulcanian (e.g., Nakada et al., 2013; Kozono et al., 2013) are also shown.

1.5 microstrains estimated from GNSS as shown by Figure 10) to cause the seismic velocity change with a typical sensitivity of seismic velocity change in a linear elastic regime (e.g., Takano et al., 2017), as discussed later, our results do not show a significant change. These observations could provide a clue for inferring the state of the material in the upper crust.

Despite of the absence of observed temporal changes for most station pairs during the 2011 eruption (Figure 9), one station pair close to the crater (SMW and SMN) showed a significant drop of seismic velocity (red lines in Figure 11). Figure 11 shows the resultant temporal variations between the station pair (SMW and SMN) from May 2010 to May 2011. The gradual drop of seismic velocity that preceded the eruption by one month. Since the station SMN was broken 10 days after the main phase of the 2011 erption, the post-eruption recovery cannot be discussed.

We discuss the 2011 Shimoedake-eruption based on the two observed temporal variations in seismic wave velocity: (i) no observed temporal variations with the one-year inflation of the magma reservoir, (ii) only the station pair close to the crater detected the gradual decrease preceding the eruption by one month.

First, we consider why the observation only shows temporal variation at one pair. Figure 12 shows areal strain, induced by the point volumetric source, by deflation caused by the migration of magma to the surface. The volumetric source modeled by Nakao et al. (2013) was located at a point (longitude 130.831°E, latitude 31.942°N, depth 8.35 km), which is about 6.9 km northwestern to Shinmoe-dake. The modeled volume change of the deflation is 13.35×10^6 m^3. This model can explain the GNSS observations during the deflation in 2011: i.e., this model can explain the observed drop of areal strain based on GNSS shown by Figure 10(b).

The typical areal strain at a depth of 3 km above the volumetric source is 5×10^{-6}, and the typical value of the bulk modulus at a depth of 3 km is 30 GPa. Since the corresponding stress change is 1.5×10^5 Pa, the stress sensitivity of seismic velocity change is estimated to be less than 6×10^{-10} Pa^{-1}. As this estimated stress sensitivity is an order of magnitude smaller than the past studies at this depth (Takano et al., 2017), our results suggest that the crustal material has lower sensitivity to static stress changes in a linear elastic regime than other regions. This observation is also consistent with that the 2016 Kumamoto earthquake caused only recovering coseismic velocity drops due to dynamic stress but no permanent ones in response to static changes in areal strain (Figure 10). The observed lack of sensitivity is also consistent with our model of precipitation effects, which does not require stress sensitivity of the seismic velocity.

One possible interpretation of the observed low sensitivity or lack of sensitivity could be related to the aspect ratio of crack and/or fluid inclusion of the medium. The low sensitivity suggests that the shape of cracks could be circular (Shapiro, 2003). The P-wave velocity at 3 km is about 5.5 km/s (Tomatsu et al., 2001), and the S-wave velocity is approximately 3.1 km/s (Nagaoka, 2020), suggesting that fraction of the geofluid and crack density should be small. The inclusions of the geofluid could also be isolated because the 3-D inversion of the anomalous magnetotelluric data in this region showed a highly resistive body above the volumetric source (Aizawa et al., 2014).

Next, we considered the spatial localization of the gradual decrease near the crater precedes the eruption by one month. For simplicity, we considered the homogeneous medium with seismic velocity c of 2 km/s, which correspond to a typical group velocity of Rayleigh waves. We evaluated the sensitivity kernel of the travel time from a point $\boldsymbol{s}_1$ to a point $\boldsymbol{s}_2$ for local changes of seismic velocities as

$$\left.\frac{\delta c(t)}{c}\right|_{app} = \frac{1}{ct}\int_S K(\boldsymbol{s}_1, \boldsymbol{s_2}, \boldsymbol{r}, t)\delta v(\boldsymbol{r})dS(\boldsymbol{r}), \tag{43}$$

where $\left.\frac{\delta c(t)}{c}\right|_{app}$ is the apparent velocity change, which corresponds to the measurement, t is travel time, $\delta v(\boldsymbol{r})$ is the perturbation of the seismic velocity at a point $\boldsymbol{r}$, S represents the whole surface area, and K is a sensitivity kernel (Pacheco & Snieder, 2005) given by,

$$K(\boldsymbol{s}_1, \boldsymbol{s_2}, \boldsymbol{r}, t) = \frac{\int_0^t p(\boldsymbol{s}_1, \boldsymbol{r}, t')p(\boldsymbol{r}, \boldsymbol{s_2}, t-t')dt'}{p(\boldsymbol{s}_1, \boldsymbol{s_2}, t)}, \tag{44}$$

where $p(\boldsymbol{s}_1, \boldsymbol{s}_2, t)$ is the probability density that the wave traveled from $\boldsymbol{s}_1$ to $\boldsymbol{s}_2$ during time t (Machacca et al., 2019): i.e. $p(\boldsymbol{s}_1, \boldsymbol{r}, t)$ satisfies the normalization condition given by,

$$\int_S p(\boldsymbol{s}_1, \boldsymbol{r}, t)dS(\boldsymbol{r}) = 1. \tag{45}$$

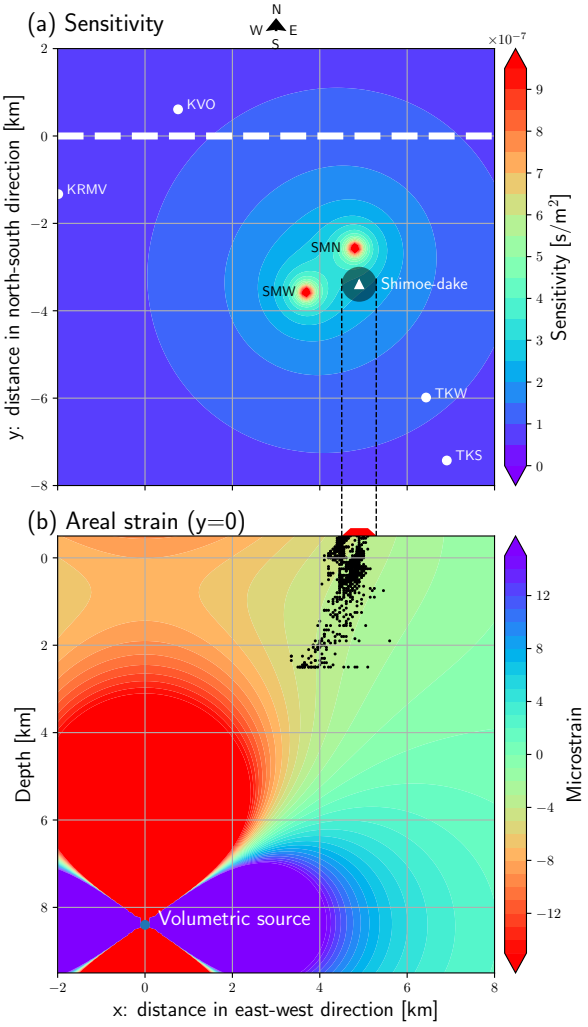

Figure 12. (a) Sensitivity kernel (Pacheco & Snieder, 2005; Obermann et al., 2013) at lapse time of 60 s. The scattering mean free path is assumed to be 5000 m. (b): Areal strain induced by the point volumetric source. The model (Nakao et al., 2013) is based on geodetic observation. This panel also shows hypocenters of volcanic tremors given by Ichihara and Matsumoto (2017). Although the hypocenters below 1 km were shifted in a westward direction, the shift might be caused by limited station coverage. We calculated the strain caused by the volumetric source using an inflation point source model (Okada, 1992) in a 3D elastic half-space with a rigidity of 10 GPa, and Poisson's ratio of 0.25. For simplicity, we assumed that the height of the surface in this area is fixed to 0.5 km above sea level.

Here p is given in the analytic form of the radiative transfer for isotropic scattering in 2-D (Obermann et al., 2013) as,

$$p(r,t) = \frac{\exp\left(-\frac{ct}{l}\right)}{2\pi r}\delta(ct-r) + \frac{1}{2\pi lct}\left(1-\frac{r^2}{c^2t^2}\right)^{-1/2}\exp\left(\frac{\sqrt{c^2t^2-r^2}-ct}{l}\right)H(ct-r), \quad (46)$$

where l is the scattering mean free path of 5000 m, r is the distance between $\boldsymbol{s}_1$ and $\boldsymbol{s}_2$, and H is the Heaviside step function. Figure 12 (a) shows the sensitivity kernel at the lapse time $t = 60$ s, which shows two local maxima at the stations. If the damaged area is 1 km at the Shinmoe-dake, which is about twice as the crater size, the velocity drop within the area is estimated to be about 5%. A trade-off exists between δc and the damaged area.

We considered three possible origins of the localized seismic velocity changes: (i) stress sensitivity of the edifice in a linear elastic regime, (ii) density perturbation due to the magma intrusion, and (iii) damage accumulation near the crater. We already showed that the stress sensitivity in this region is small, though past studies (e.g., Sens-Schönfelder et al., 2014) have shown that stress changes due to the increased pressure of the magma reservoir could cause the observable seismic velocity change. Moreover, no other inflation/deflation sources were observed before the 2011 Shinmoe-dake eruption. Next, we considered density perturbation, as in the case of the precipitation effect. Kozono et al. (2013) estimated the erupted volume based on geodetic and satellite observations. The total extruded volume of dense rock equivalence was estimated to about 3×10^7 m^3, and the density was 2500 kg/m^3. In order to constrain the upper limit of seismic velocity reduction due the density perturbation, we assumed that the magma was stored at a depth shallower than 0.6 km where Rayleigh waves have the greater sensitivity (Figure 5). The equation (38) leads to the upper limit of about 0.6% drop in seismic velocity, which is significantly smaller than our observations (5%). Therefore we conclude that the observed seismic velocity drop with a time scale of about one month near the crater could be caused by cumulative damage beyond the linear elastic regime, induced by the pressure exerted by the magma reservoir on the edifice (Olivier et al., 2019).

The location of the volcanic tremor (TR) source also gives us a clue as to the magma or gas movement before the main eruption. Ichihara and Matsumoto (2017) located TR sources from seven stations recording continuous volcanic tremor before and during the sub-Plinian eruptions using the amplitude distribution. Figure 11(b) shows the source depth of TR from January 3rd, 2011, to February 2nd, 2011. Prior to January 2011, the TR amplitudes were too small to locate. Before the precursory stage of the eruption, the source depths were approximately 2 km. With increased damage, the source depth migrated upward to around sea level when the precursory stage was initiated. When the sub-Plinian eruption started, the decreasing rate of seismic velocity changes became steeper. This observation suggests that the magma migration from 2 km to the surface increased the damage of the sub-surface material. Figure 12(b) shows the depth section of the source locations. They also support the vertical magma migration beneath the summit. The sources below 1 km could be biased in the western direction, due to the limited station distribution.

Ambient noise tomography in this region (Nagaoka, 2020) revealed the magma reservoir imaged as a low S-wave velocity body with a strong radial anisotropy of up to 30%. It was located just below the geodetic source, and the horizontal scale was about 15 km (Figure 13). Horizontally multilayered sills can explain the strong radial anisotropy with and without partial melts. The connection between the sills can enable the horizontal magma migration from the magma reservoir to Shinmoe-dake. The geochemical analysis (Nakada et al., 2013; Suzuki et al., 2013) showed the basaltic magma was stored at the magma reservoir. The viscosity is low enough to develop the sill complex, and the mobility is high during the eruption. In January 2011, due to damage, the pressurization of the magma began to decrease the seismic velocity gradually. The pressurization

also activated TR activity at depth of 2 km (Figure 13(a)). During this stage, the silicic magma was mixed with the basaltic magma (Suzuki et al., 2013). Since the viscosity of the silicic magma is estimated to be high (about 1.2×10^6 Pa·s, Suzuki et al., 2013), the magma fluid could be isolated.

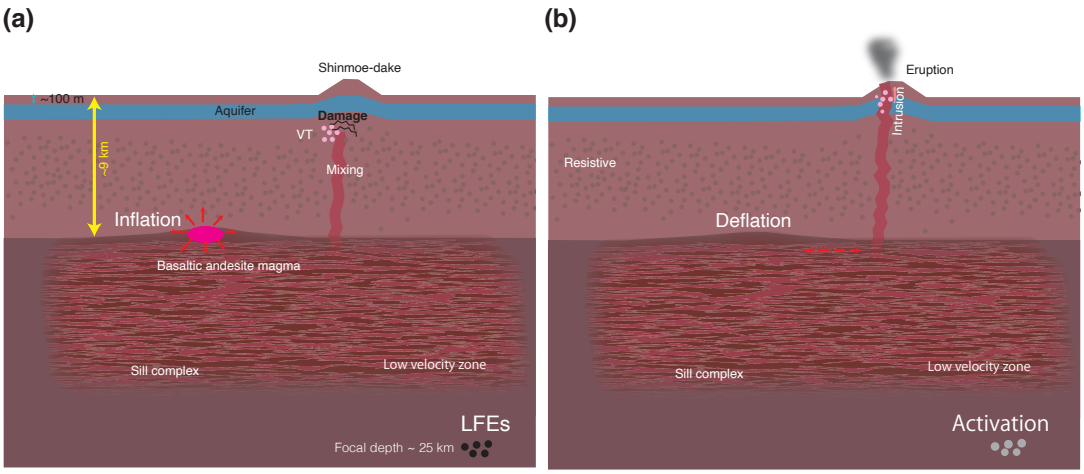

Figure 13. Schematic of the 2011 eruption: (a) from one month before until just before the eruption, and (b) during the eruption. LFEs represent low frequency earthquakes (Kurihara et al., 2019), and TR represents volcanic tremor (Ichihara & Matsumoto, 2017).

8 Conclusions

In this study, seismic interferometry was applied to a seismic network around Shinmoe-dake to monitor the seismic velocity change for eight years from May 2010 to April 2018. We applied the stretching method (Sens-Schönfelder & Wegler, 2006) for a cross-correlation function calculated for each pair of stations using continuous ambient noise data. To separate the variations of volcanic origin from environmental variations, we developed a new technique based on a state-space model: the parameters (e.g., seismic velocity change) were estimated by an extended Kalman filter, and the hyper-parameters (the seismic response to the precipitation, the response to the Kumamoto earthquake, and covariances of the parameters) were estimated by the Maximum Likelihood Method. The resultant seismic velocity changes show clear seasonal variation originating from precipitation as well as a drop associated with the 2016 Kumamoto earthquake.

After the effects of precipitation and the earthquake were subtracted, most of the seismic velocity changes did not show any changes associated with the eruptions. Since the strain changes caused by the volumetric change during the 2011 eruption (Nakao et al., 2013) were about five microstrains at depths from 0 to 2 km above the source, the stress sensitivity of the seismic velocity in a linear elastic regime was significantly smaller than other areas (e.g. Takano et al., 2017). The observed lack of sensitivity suggests the smaller aspect ratio of crack and less fluid inclusion in the upper crust (Shapiro, 2003), which is consistent with the highly resistive body above the volumetric source(Aizawa et al., 2014). The P-wave velocity at 3 km is about 5.5 km/s (Tomatsu et al., 2001), and the S-wave velocity is about 3.1 km/s (Nagaoka, 2020), indicating small melt fraction and crack density.

Only one station pair located in the neighborhood of the crater showed a gradual decrease in seismic velocity, which preceded the eruption by one month. The maximum drop of the seismic velocity was about 0.05% during the 2011 eruption. The sensitivity kernel (Pacheco & Snieder, 2005) of this observation suggests that the seismic wave drop of about 5% was localized at the crater with a spatial dimension of about one km^2. In this region, P wave travel time tomography revealed a pipe-like structure of high-velocity under the summit craters from 1.5 to 0.5 km below sea level (Tomatsu et al., 2001). The fluid intrusion started to damage the high-velocity pipe structure one month before the eruption. Until January 16th 2011, the source depths of TR were around 2 km (Ichihara & Matsumoto, 2017) although the TR amplitudes were too small to locate before January 2011. With increasing damage, the source depth migrated upward to around sea level when the precursory stage started on January 16th. Then, the magma migrated from the depth of 2 km to the surface. The magma migrated vertically from the reservoir imaged as a low S-wave velocity body just below the geodetic source.

Notation

$\boldsymbol{t}$**:** Days from 1 May 2010 (JST) $= 1, \ldots, n$
$\boldsymbol{p}$**:** A component pair (9 components: $R-R$, $R-T$, ..., $Z-Z$).
$\boldsymbol{\tau}$**:** Lag time of a CCF
$\boldsymbol{\phi_t^p(\tau)}$**:** Observed CCF
$\boldsymbol{y_t^p}$**:** The data vector consisting of $\phi_t^p, \tau = (-\tau_e, -\tau_e + 1 \cdots - \tau_s, \tau_s \tau_s + 1 \cdots \tau_e)$
$\boldsymbol{\alpha_t \equiv (A_t, \gamma_t)^T}$**:** The state variable $\boldsymbol{\alpha}_t$ with the amplitude A_t and stretching factor γ_t
$\boldsymbol{R_t \equiv (0, r_t)^T}$**:** Explanatory variables related to precipitation, where r_t explains the stretching factor
$\boldsymbol{E_t \equiv (0, e_t)^T}$**:** Explanatory variables associated with the 2016 Kumamoto earthquake, where e_t explains the stretching factor
$\boldsymbol{m^p(A_t, \gamma_t; \tau)}$**:** a model of an observed CCF
$\boldsymbol{\varphi_{ref}^p(\tau)}$**:** The reference CCF
$\boldsymbol{H_t \equiv h_0 I}$**:** A prior data covariance matrix, where h_0 is a prior data covariance
$\boldsymbol{I}$**:** Identity matrix
$\boldsymbol{Q_t}$**:** A prior model covariance matrix
$\boldsymbol{a_1 \equiv (A_1, \gamma_1)^T}$**:** A prior initial value of the state variable
$\boldsymbol{P_1}$**:** A prior model covariance matrix of the initial value

Acknowledgments
I am grateful to people for maintaining the networks and making the data readily available. This work was supported by JSPS KAKENHI Grant Number JP17H02950 and JP17K05625. This research made use of ObsPy (Krischer et al., 2015), NumPy (Van Der Walt et al., 2011) and SciPy (Virtanen et al., 2019). Figure 1 was prepared with GMT programs (Wessel et al., 2013). We thank M. Takeo, Y. Takei and T. Ohminato for the valuable discussions. We also thank Nori Nakata, Julien Chaput and Rick Aster for their helpful and constructive feedback that has improved this manuscript.

Data and materials availability:

We used data from F-net (`doi.org/10.17598/nied.0005`), Hi-net (`doi.org/10.17598/nied.0003`), V-net (`doi.org/10.17598/nied.0006`) and K-net (`doi.org/10.17598/nied.0004`), which are managed by the National Research Institute for Earth Science and Disaster Prevention (NIED), Japan. In situ precipitation observations were obtained from the Automated Meteorological Data Acquisition System (AMeDAS) of the Japan Meteorological Agency (JMA) are available at `http://www.data.jma.go.jp/`

`obd/stats/etrn/index.php` (in Japanese). F3 solutions of GNSS data are provided by Geospatial Information Authority of Japan (`http://www.gsi.go.jp`). Daily CCFs in this study are available at zenodo (10.5281/zenodo.2539824). The python code is also available at `https://github.com/qnishida/eKlf_SI`.

References

Aizawa, K., Koyama, T., Hase, H., Uyeshima, M., Kanda, W., Utsugi, M., ... Ogawa, Y. (2014). Three-dimensional resistivity structure and magma plumbing system of the Kirishima Volcanoes as inferred from broadband magnetotelluric data. *Journal of Geophysical Research: Solid Earth*, *119*(1), 198–215. doi: 10.1002/2013JB010682

Akaike, H. (1974). A New Look at the Statistical Model Identification. *IEEE Transactions on Automatic Control*, *19*(6), 716–723. doi: 10.1109/TAC.1974.1100705

Aoki, Y., Segall, P., Kato, T., Cervelli, P., & Shimada, S. (1999). Imaging magma transport during the 1997 seismic swarm off the Izu Peninsula, Japan. *Science*, *286*(5441), 927–930. doi: 10.1126/science.286.5441.927

Bensen, G. D., Ritzwoller, M. H., Barmin, M. P., Levshin, A. L., Lin, F., Moschetti, M. P., ... Yang, Y. (2007). Processing seismic ambient noise data to obtain reliable broad-band surface wave dispersion measurements. *Geophysical Journal International*, *169*(3), 1239–1260. doi: 10.1111/j.1365-246X.2007.03374.x

Brenguier, F., Campillo, M., Hadziioannou, C., Shapiro, N., Nadeau, R. M., & Larose, E. (2008). Postseismic relaxation along the san andreas fault at parkfield from continuous seismological observations. *Science*, *321*(5895), 1478–1481.

Brenguier, F., Campillo, M., Takeda, T., Aoki, Y., Shapiro, N. M., Briand, X., ... Miyake, H. (2014). Mapping pressurized volcanic fluids from induced crustal seismic velocity drops. *Science*, *345*(6192), 80–82. doi: 10.1126/science.1254073

Brenguier, F., Rivet, D., Obermann, A., Nakata, N., Bouoé, P., Lecocq, T., ... Shapiro, N. (2016). 4-D noise-based seismology at volcanoes: Ongoing efforts and perspectives. *Journal of Volcanology and Geothermal Research*, *321*, 182–195. doi: 10.1016/j.jvolgeores.2016.04.036

Brenguier, F., Shapiro, N. M., Campillo, M., Ferrazzini, V., Duputel, Z., Coutant, O., & Nercessian, A. (2008). Towards forecasting volcanic eruptions using seismic noise. *Nature Geoscience*, *1*(2), 126–130. doi: 10.1038/ngeo104

Budi-Santoso, A., & Lesage, P. (2016). Velocity variations associated with the large 2010 eruption of Merapi volcano, Java, retrieved from seismic multiplets and ambient noise cross-correlation. *Geophysical Journal International*, *206*(1), 221–240. doi: 10.1093/gji/ggw145

Colombi, A., Chaput, J., Brenguier, F., Hillers, G., Roux, P., & Campillo, M. (2014). On the temporal stability of the coda of ambient noise correlations. *Comptes Rendus - Geoscience*, *346*(11-12), 307–316. doi: 10.1016/j.crte.2014.10.002

Donaldson, C., Caudron, C., Green, R. G., Thelen, W. A., & White, R. S. (2017). Relative seismic velocity variations correlate with deformation at Klauea volcano. *Science Advances*, *3*(6), e1700219. doi: 10.1126/sciadv.1700219

Durbin, J., & Koopman, S. J. (2012). *Time Series Analysis by State Space Methods* (Second ed.). Oxford University Press. doi: 10.1093/acprof:oso/9780199641178.001.0001

Farr, T. G., Rosen, P. A., Caro, E., Crippen, R., Duren, R., Hensley, S., ... Alsdorf, D. (2007). The Shuttle Radar Topography Mission. *Review of Geophysics*, *45*(2), RG2004. doi: 10.1029/2005RG000183

Gassenmeier, M., Sens-Schönfelder, C., Eulenfeld, T., Bartsch, M., Victor, P.,

Tilmann, F., & Korn, M. (2016). Field observations of seismic velocity changes caused by shaking-induced damage and healing due to mesoscopic nonlinearity. *Geophysical Journal International*, *204*(3), 1490–1502. doi: 10.1093/gji/ggv529

Gomberg, J., & Agnew, D. (1996). The accuracy of seismic estimates of dynamic strains: An evaluation using strainmeter and seismometer data from Piñon Flat Observatory, California. *Bulletin of the Seismological Society of America*, *86*(1 SUPPL. A), 212–220.

Hendriyana, A., & Tsuji, T. (2019). Migration of Very Long Period Seismicity at Aso Volcano, Japan, Associated With the 2016 Kumamoto Earthquake. *Geophysical Research Letters*, *46*(15), 8763–8771. doi: 10.1029/2019GL082645

Hillers, G., Ben-Zion, Y., Campillo, M., & Zigone, D. (2015). Seasonal variations of seismic velocities in the San Jacinto fault area observed with ambient seismic noise. *Geophysical Journal International*, *202*(2), 920–932. doi: 10.1093/gji/ggv151

Hillers, G., Husen, S., Obermann, A., Planès, T., Larose, E., & Campillo, M. (2015). Noise-based monitoring and imaging of aseismic transient deformation induced by the 2006 Basel reservoir stimulation. *Geophysics*, *80*(4), KS51–KS68. doi: 10.1190/geo2014-0455.1

Hobiger, M., Wegler, U., Shiomi, K., & Nakahara, H. (2016). Coseismic and post-seismic velocity changes detected by passive image interferometry: Comparison of one great and five strong earthquakes in Japan. *Geophysical Journal International*, *205*(2), 1053–1073. doi: 10.1093/gji/ggw066

Ichihara, M., & Matsumoto, S. (2017). Relative Source Locations of Continuous Tremor Before and After the Subplinian Events at Shinmoe-dake, in 2011. *Geophysical Research Letters*, *44*(21), 10,871–10,877. doi: 10.1002/2017GL075293

Kagiyama, T., Utada, H., Uyeshima, M., Masutani, F., Kanda, W., Tanaka, Y., ... Mishina, M. (1996). Resistivity Structure of the Central and the Southeastern Part of Kirishima Volcanoes. *Bulltin of the volcanological society of Japan*, *41*(5), 215–225. doi: 10.18940/kazan.41.5_215

Kaneshima, S., Kawakatsu, H., Matsubayashi, H., Sudo, Y., Tsutsui, T., Ohminato, T., ... Iidaka, T. (1996). Mechanism of Phreatic Eruptions at Aso Volcano Inferred from Near-Field Broadband Seismic Observations. *Science*, *273*(5275), 643–645. doi: 10.1126/science.273.5275.643

Kato, A., Nakamura, K., & Hiyama, Y. (2016). The 2016 Kumamoto earthquake sequence. *Proceedings of the Japan Academy Series B: Physical and Biological Sciences*, *92*(8), 358–371. doi: 10.2183/pjab.92.359

Kim, D., & Lekic, V. (2019). Groundwater Variations From Autocorrelation and Receiver Functions. *Geophysical Research Letters*, 722–729. doi: 10.1029/2019GL084719

Kozono, T., Ueda, H., Ozawa, T., Koyaguchi, T., Fujita, E., Tomiya, A., & Suzuki, Y. J. (2013). Magma discharge variations during the 2011 eruptions of Shinmoe-dake volcano, Japan, revealed by geodetic and satellite observations. *Bull. Volcanol.*, *75*(3), 1–13. doi: 10.1007/s00445-013-0695-4

Krischer, L., Megies, T., Barsch, R., Beyreuther, M., Lecocq, T., Caudron, C., & Wassermann, J. (2015). ObsPy: A bridge for seismology into the scientific Python ecosystem. *Computational Science and Discovery*, *8*(1). doi: 10.1088/1749-4699/8/1/014003

Kurihara, R., Obara, K., Takeo, A., & Tanaka, Y. (2019). Deep Low-Frequency Earthquakes Associated With the Eruptions of Shinmoe-dake in KirishimaVolcanoes. *Journal of Geophysical Research: Solid Earth*, 2019JB018032. doi: 10.1029/2019JB018032

Lecocq, T., Longuevergne, L., Pedersen, H. A., Brenguier, F., & Stammler, K. (2017). Monitoring ground water storage at mesoscale using seismic noise:

30 years of continuous observation and thermo-elastic and hydrological modeling. *Sci. Rep.*, *7*(1), 1–16. doi: 10.1038/s41598-017-14468-9

Machacca, R., Lesage, P., Larose, E., Lacroix, P., & Anccasi, R. (2019). Detection of pre-eruptive seismic velocity variations at an andesitic volcano using ambient noise correlation on 3-component stations: Ubinas volcano, Peru, 2014. *Journal of Volcanology and Geothermal Research*. doi: 10.1016/j.jvolgeores.2019.05.014

Maeda, T., Obara, K., Furumura, T., & Saito, T. (2011). Interference of long-period seismic wavefield observed by dense hi-net array in japan. *Journal of Geophysical Research*, *116*.

Malinverno, A., & Briggs, V. A. (2004). Expanded uncertainty quantification in inverse problems: Hierarchical Bayes and empirical Bayes. *Geophysics*, *69*(4), 1005–1016. doi: 10.1190/1.1778243

Miyazawa, M. (2011). Propagation of an earthquake triggering front from the 2011 Tohoku-Oki earthquake. *Geophysical Research Letters*, *38*(23), n/a–n/a. doi: 10.1029/2011GL049795

Nagaoka, Y. (2020). *Study on seismic velocity structure beneath active volcanoes by seismic interferometry* (PhD). The university of Tokyo.

Nagaoka, Y., Nishida, K., Aoki, Y., & Takeo, M. (2010). Temporal change of phase velocity beneath Mt. Asama, Japan, inferred from coda wave interferometry. *Geophysical Research Letters*, *37*(22), 1–5. doi: 10.1029/2010GL045289

Nakada, S., Nagai, M., Kaneko, T., Suzuki, Y., & Maeno, F. (2013). The outline of the 2011 eruption at Shinmoe-dake (Kirishima), Japan. *Earth, Planets and Space*, *65*(6), 475–488. doi: 10.5047/eps.2013.03.016

Nakamichi, H., Yamanaka, Y., Terakawa, T., Horikawa, S., Okuda, T., & Yamazaki, F. (2013). Continuous long-term array analysis of seismic records observed during the 2011 Shinmoedake eruption activity of Kirishima volcano, southwest Japan. *Earth, Planets and Space*, *65*(6), 551–562. doi: 10.5047/eps.2013.03.002

Nakao, S., Morita, Y., Yakiwara, H., Oikawa, J., Ueda, H., Takahashi, H., ... Iguchi, M. (2013). Volume change of the magma reservoir relating to the 2011 Kirishima Shinmoe-dake eruption—Charging, discharging and recharging process inferred from GPS measurements. *Earth, Planets and Space*, *65*(6), 505–515. doi: 10.5047/eps.2013.05.017

Nimiya, H., Ikeda, T., & Tsuji, T. (2017). Spatial and temporal seismic velocity changes on Kyushu Island during the 2016 Kumamoto earthquake. *Science Advances*, *3*(11), e1700813. doi: 10.1126/sciadv.1700813

Nishida, K., Kawakatsu, H., & Obara, K. (2008). Three-dimensional crustal S wave velocity structure in Japan using microseismic data recorded by Hi-net tiltmeters. *Journal of Geophysical Research: Solid Earth*, *113*(B10), B10302. doi: 10.1029/2007JB005395

Niu, F., Silver, P. G., Daley, T. M., Cheng, X., & Majer, E. L. (2008). Preseismic velocity changes observed from active source monitoring at the parkfield safod drill site. *Nature*, *454*(7201), 204.

Obermann, A., & Hillers, G. (2019). Chapter Two - Seismic time-lapse interferometry across scales. In C. Schmelzbach (Ed.), *Advances in seismology* (Vol. 60, pp. 65–143). Elsevier. doi: 10.1016/bs.agph.2019.06.001

Obermann, A., Planes, T., Larose, E., Sens-Schonfelder, C., & Campillo, M. (2013). Depth sensitivity of seismic coda waves to velocity perturbations in an elastic heterogeneous medium. *Geophysical Journal International*, *194*(1), 372–382. doi: 10.1093/gji/ggt043

Ogiso, M., Yomogida, K., & Katsumata, K. (2005). Recursive travel-time inversion: A tool for real-time seismic tomography. *Earth, Planets Sp.*, *57*(6), 477–489. doi: 10.1186/BF03352582

Okada, Y. (1992). Internal deformation due to shear and tensile faults in a half-

space. *Bulletin - Seismological Society of America*, *82*(2), 1018–1040.
Olivier, G., Brenguier, F., Carey, R., Okubo, P., & Donaldson, C. (2019). Decrease in Seismic Velocity Observed Prior to the 2018 Eruption of Klauea Volcano With Ambient Seismic Noise Interferometry. *Geophysical Research Letters*, *46*(7), 3734–3744. doi: 10.1029/2018GL081609
Pacheco, C., & Snieder, R. (2005). Time-lapse travel time change of multiply scattered acoustic waves. *The Journal of the Acoustical Society of America*, *118*(3), 1300–1310. doi: 10.1121/1.2000827
Poupinet, G., Ellsworth, W., & Frechet, J. (1984). Monitoring velocity variations in the crust using earthquake doublets: An application to the calaveras fault, california. *Journal of Geophysical Research: Solid Earth*, *89*(B7), 5719–5731.
Rivet, D., Brenguier, F., & Cappa, F. (2015). Improved detection of preeruptive seismic velocity drops at the Piton de La Fournaise volcano. *Geophysical Research Letters*, 1–8. doi: 10.1002/2015GL064835.Received
Rivet, D., Campillo, M., Shapiro, N. M., Cruz-Atienza, V., Radiguet, M., Cotte, N., & Kostoglodov, V. (2011). Seismic evidence of nonlinear crustal deformation during a large slow slip event in Mexico. *Geophysical Research Letters*, *38*(8), 3–7. doi: 10.1029/2011GL047151
Sandanbata, O., Obara, K., Maeda, T., Takagi, R., & Satake, K. (2015). Sudden changes in the amplitude-frequency distribution of long-period tremors at Aso volcano, southwest Japan. *Geophysical Research Letters*, *42*(23), 10256–10262. doi: 10.1002/2015GL066443
Segall, P., & Matthews, M. (1997). Time dependent inversion of geodetic data. *Journal of Geophysical Research: Solid Earth*, *102*(B10), 22391–22409. doi: 10.1029/97JB01795
Sens-Schönfelder, C., & Eulenfeld, T. (2019). Probing the in situ Elastic Nonlinearity of Rocks with Earth Tides and Seismic Noise. *Phys. Rev. Lett.*, *122*(13), 138501. doi: 10.1103/PhysRevLett.122.138501
Sens-Schönfelder, C., Pomponi, E., & Peltier, A. (2014). Dynamics of Piton de la Fournaise volcano observed by passive image interferometry with multiple references. *Journal of Volcanology and Geothermal Research*, *276*, 32–45. doi: 10.1016/j.jvolgeores.2014.02.012
Sens-Schönfelder, C., & Wegler, U. (2006). Passive image interferemetry and seasonal variations of seismic velocities at Merapi Volcano, Indonesia. *Geophysical Research Letters*, *33*(21), 1–5. doi: 10.1029/2006GL027797
Shapiro, S. A. (2003). Elastic piezosensitivity of porous and fractured rocks. *Geophysics*, *68*(2), 482–486. doi: 10.1190/1.1567215
Snieder, R., Sens-Schönfelder, C., & Wu, R. (2017). The time dependence of rock healing as a universal relaxation process, a tutorial. *Geophysical Journal International*, *208*(1), 1–9. doi: 10.1093/gji/ggw377
Suzuki, Y., Yasuda, A., Hokanishi, N., Kaneko, T., Nakada, S., & Fujii, T. (2013). Syneruptive deep magma transfer and shallow magma remobilization during the 2011 eruption of Shinmoe-dake, Japan-Constraints from melt inclusions and phase equilibria experiments. *Journal of Volcanology and Geothermal Research*, *257*, 184–204. doi: 10.1016/j.jvolgeores.2013.03.017
Takano, T., Nishimura, T., & Nakahara, H. (2017). Seismic velocity changes concentrated at the shallow structure as inferred from correlation analyses of ambient noise during volcano deformation at Izu-Oshima, Japan. *Journal of Geophysical Research: Solid Earth*, *122*(8), 6721–6736. doi: 10.1002/2017JB014340
Takano, T., Nishimura, T., Nakahara, H., Ohta, Y., & Tanaka, S. (2014). Seismic velocity changes caused by the Earth tide: Ambient noise correlation analyses of small-array data. *Geophysical Research Letters*, *41*(17), 6131–6136. doi: 10.1002/2014GL060690
Takano, T., Nishimura, T., Nakahara, H., Ueda, H., & Fujita, E. (2019). Sensitivity of Seismic Velocity Changes to the Tidal Strain at Different Lapse

Times: Data Analyses of a Small Seismic Array at Izu-Oshima Volcano. *Journal of Geophysical Research: Solid Earth*, *124*(3), 3011–3023. doi: 10.1029/2018JB016235

Takeo, M., Maehara, Y., Ichihara, M., Ohminato, T., Kamata, R., & Oikawa, J. (2013). Ground deformation cycles in a magma-effusive stage, and sub-Plinian and Vulcanian eruptions at Kirishima volcanoes, Japan. *Journal of Geophysical Research: Solid Earth*, *118*(9), 4758–4773. doi: 10.1002/jgrb.50278

Takeuchi, H., & Saito, M. (1972). Seismology: Surface Waves and Free Oscillations. In B. A. Bolt (Ed.), *Methos in computational physics* (Vol. 11, pp. 217–295). Academic Press, New York.

Talwani, P., Chen, L., & Gahalaut, K. (2007). Seismogenic permeability, ks. *Journal of Geophysical Research: Solid Earth*, *112*(B7).

Tarantola, A., & Valette, B. (1982). Generalized nonlinear inverse problems solved using the least squares criterion. *Reviews of Geophysics*, *20*(2), 219. doi: 10.1029/RG020i002p00219

Tomatsu, T., Kumagai, H., & Dawson, P. B. (2001). Tomographic inversion of P-wave velocity and Q structures beneath the Kirishima volcanic complex, Southern Japan, based on finite difference calculations of complex traveltimes. *Geophysical Journal International*, *146*(3), 781–794. doi: 10.1046/j.1365-246X.2001.00491.x

Tsukamoto, K., Aizawa, K., Chiba, K., Kanda, W., Uyeshima, M., Koyama, T., ... Kishita, T. (2018). Three-Dimensional Resistivity Structure of Iwo-Yama Volcano, Kirishima Volcanic Complex, Japan: Relationship to Shallow Seismicity, Surface Uplift, and a Small Phreatic Eruption. *Geophysical Research Letters*, *45*(23), 12,821–12,828. doi: 10.1029/2018GL080202

Ueda, H., Kozono, T., Fujita, E., Kohno, Y., Nagai, M., Miyagi, Y., & Tanada, T. (2013). Crustal deformation associated with the 2011 Shinmoe-dake eruption as observed by tiltmeters and GPS. *Earth, Planets and Space*, *65*(6), 517–525. doi: 10.5047/eps.2013.03.001

Van Der Walt, S., Colbert, S. C., & Varoquaux, G. (2011). The numpy array: a structure for efficient numerical computation. *Computing in Science & Engineering*, *13*(2), 22–30.

Virtanen, P., Gommers, R., Oliphant, T. E., Haberland, M., Reddy, T., Cournapeau, D., ... Contributors, S. . . (2019). SciPy 1.0–Fundamental Algorithms for Scientific Computing in Python. *arXiv e-prints*, arXiv:1907.10121.

Wang, Q.-Y., Brenguier, F., Campillo, M., Lecointre, A., Takeda, T., & Aoki, Y. (2017). Seasonal crustal seismic velocity changes throughout Japan. *Journal of Geophysical Research: Solid Earth*, *122*(10), 7987-8002. doi: 10.1002/2017JB014307

Wang, Q. Y., Campillo, M., Brenguier, F., Lecointre, A., Takeda, T., & Hashima, A. (2019). Evidence of Changes of Seismic Properties in the Entire Crust Beneath Japan After the Mw 9.0, 2011 Tohoku-oki Earthquake. *Journal of Geophysical Research: Solid Earth*, *124*(8), 8924–8941. doi: 10.1029/2019JB017803

Weaver, R., Froment, B., & Campillo, M. (2009). On the correlation of non-isotropically distributed ballistic scalar diffuse waves. *The Journal of the Acoustical Society of America*, *126*(4), 1817–26. doi: 10.1121/1.3203359

Weaver, R., Hadziioannou, C., Larose, E., & Campillo, M. (2011). On the precision of noise correlation interferometry. *Geophysical Journal International*, *185*(3), 1384–1392. doi: 10.1111/j.1365-246X.2011.05015.x

Weaver, R., & Lobkis, O. (2000). Temperature dependence of diffuse field phase. *Ultrasonics*, *38*(1), 491–494. doi: 10.1016/S0041-624X(99)00047-5

Wegler, U., Nakahara, H., Sens-Schönfelder, C., Korn, M., & Shiomi, K. (2009). Sudden drop of seismic velocity after the 2004 Mw 6.6 mid-Niigata earthquake, Japan, observed with Passive Image Interferometry B06305. *Journal of Geophysical Research: Solid Earth*, *114*(6), 1–11. doi: 10.1029/2008JB005869

Wegler, U., & Sens-Schönfelder, C. (2007). Fault zone monitoring with passive image interferometry. *Geophysical Journal International*, *168*(3), 1029–1033.

Wessel, P., Smith, W. H. F., Scharroo, R., Luis, J., & Wobbe, F. (2013). Generic mapping tools: Improved version released. *Eos, Transactions American Geophysical Union*, *94*(45), 409-410. doi: 10.1002/2013EO450001

Yamada, T., Ueda, H., Mori, T., & Tanada, T. (2019). Tracing Volcanic Activity Chronology from a Multiparameter Dataset at Shinmoedake Volcano (Kirishima), Japan. *Journal of Disaster Research*, *14*(5), 687–700. doi: 10.20965/jdr.2019.p0687

Yamamura, K., Sano, O., Utada, H., Takei, Y., Nakao, S., & Fukao, Y. (2003). Long-term observation of in situ seismic velocity and attenuation. *Journal of Geophysical Research: Solid Earth*, *108*(B6), 1–15. doi: 10.1029/2002JB002005

Zhu, C., Byrd, R. H., Lu, P., & Nocedal, J. (1994). Fortran subroutines for large-scale bound constrained optimization. *ACM Trans Math Softw*, *23*(4), 550–60.

Appendix A Calculation of the likelihood

For an efficient evaluation of the likelihood defined by equation (32), calculation of the determinant of a large matrix $\boldsymbol{F}_t$ ($N \times N$ matrix) becomes the bottleneck. To reduce the calculations, we rewrote the definition of the likelihood as follows. Since $\boldsymbol{Z}_t \hat{\boldsymbol{P}}_{t|t-1} \boldsymbol{Z}_t^T$ is the symmetric matrix, it can be diagonalized by the unitary matrix $\boldsymbol{U}$ as

$$\boldsymbol{U}^t \boldsymbol{F}_t \boldsymbol{U} = \boldsymbol{\Lambda}, \tag{A1}$$

where the eigen matrix $\boldsymbol{\Lambda}$ can be written

$$\Lambda \equiv \begin{pmatrix} \lambda_1 & 0 & 0 & \cdots & 0 \\ 0 & \lambda_2 & 0 & \cdots & 0 \\ 0 & 0 & 0 & \cdots & 0 \\ \vdots & \vdots & \vdots & \ddots & 0 \\ 0 & 0 & 0 & \cdots & 0 \end{pmatrix}, \tag{A2}$$

Since the rank of $\boldsymbol{Z}_t \hat{\boldsymbol{P}}_{t|t-1} \boldsymbol{Z}_t^T$ is 2, the other $N-2$ eigen values are zeros.

Then the determinant can be written by

$$\det(\boldsymbol{F}_t) = \det(\boldsymbol{U}^T \boldsymbol{F}_t \boldsymbol{U}) = \det(\Lambda + h_0 \boldsymbol{I}) = (\lambda_1 + h_0)(\lambda_2 + h_0) h_0^{N-2}. \tag{A3}$$

Here we consider the eigen values of $\boldsymbol{Z}_t \hat{\boldsymbol{P}}_{t|t-1} \boldsymbol{Z}_t^T$. For a given eigen vector $\boldsymbol{x_i}$ for eigen value λ_i,

$$\boldsymbol{Z}_t \hat{\boldsymbol{P}}_{t|t-1} \boldsymbol{Z}_t^T \boldsymbol{x} = \lambda_i \boldsymbol{x}_i. \tag{A4}$$

Multiply both sides of each equation by $\boldsymbol{Z}_t$

$$\boldsymbol{Z}_t^T \boldsymbol{Z}_t \hat{\boldsymbol{P}}_{t|t-1} \boldsymbol{Z}_t^T \boldsymbol{x} = \lambda_i \boldsymbol{Z}_t^T \boldsymbol{x}_i. \tag{A5}$$

Since this equation can be interpreted as an eigen value problem for the smaller matrix $\boldsymbol{Z}_t^T \boldsymbol{Z}_t \hat{\boldsymbol{P}}_{t|t-1}$ (2×2 matrix), we can obtain these efficiently.